01 Apr 2016

Evolution of Stellar-To-Halo Mass Ratio at Z = 0-7 Identified by Clustering Analysis with the Hubble Legacy Imaging and Early Subaru/Hyper Suprime-Cam Survey Data

Yuichi Harikane

Masami Ouchi

Yoshiaki Ono

Surhud More

et. al. For a complete list of authors, see https://scholarsmine.mst.edu/phys_facwork/1949

Recommended Citation

Y. Harikane et al., "Evolution of Stellar-To-Halo Mass Ratio at Z = 0-7 Identified by Clustering Analysis with the Hubble Legacy Imaging and Early Subaru/Hyper Suprime-Cam Survey Data," *Astrophysical Journal*, vol. 821, no. 2, Institute of Physics - IOP Publishing, Apr 2016.
The definitive version is available at https://doi.org/10.3847/0004-637X/821/2/123

The Astrophysical Journal, 821:123 (23pp), 2016 April 20 doi:10.3847/0004-637X/821/2/123

EVOLUTION OF STELLAR-TO-HALO MASS RATIO AT $z = 0$–7 IDENTIFIED BY CLUSTERING ANALYSIS WITH THE HUBBLE LEGACY IMAGING AND EARLY SUBARU/HYPER SUPRIME-CAM SURVEY DATA

Yuichi Harikane[1,2], Masami Ouchi[1,3], Yoshiaki Ono[1], Surhud More[3], Shun Saito[3], Yen-Ting Lin[4], Jean Coupon[5], Kazuhiro Shimasaku[6,7], Takatoshi Shibuya[1], Paul A. Price[8], Lihwai Lin[4], Bau-Ching Hsieh[4], Masafumi Ishigaki[1,2], Yutaka Komiyama[9], John Silverman[3], Tadafumi Takata[9], Hiroko Tamazawa[1,2], and Jun Toshikawa[9]
[1] Institute for Cosmic Ray Research, The University of Tokyo, 5-1-5 Kashiwanoha, Kashiwa, Chiba 277-8582, Japan; hari@icrr.u-tokyo.ac.jp
[2] Department of Physics, Graduate School of Science, The University of Tokyo, 7-3-1 Hongo, Bunkyo, Tokyo, 113-0033, Japan
[3] Kavli Institute for the Physics and Mathematics of the Universe (Kavli IPMU, WPI), University of Tokyo, Kashiwa, Chiba 277-8583, Japan
[4] Institute of Astronomy & Astrophysics, Academia Sinica, Taipei 106, Taiwan (ROC)
[5] Astronomical Observatory of the University of Geneva, ch. dEcogia 16, 1290 Versoix, Switzerland
[6] Department of Astronomy, Graduate School of Science, The University of Tokyo, Hongo, Bunkyo, Tokyo 113-0033, Japan
[7] Research Center for the Early Universe, The University of Tokyo, Hongo, Tokyo 113-0033, Japan
[8] Princeton University Observatory, Peyton Hall, Princeton, NJ 08544, USA
[9] National Astronomical Observatory, Mitaka, Tokyo 181-8588, Japan
Received 2015 November 24; accepted 2016 March 2; published 2016 April 20

ABSTRACT

We present clustering analysis results from 10,381 Lyman break galaxies (LBGs) at $z \sim 4$–7, identified in the *Hubble* legacy deep imaging and new complimentary large-area Subaru/Hyper Suprime-Cam data. We measure the angular correlation functions of these LBGs at $z \sim 4$, 5, 6, and 7 and fit these measurements using halo occupation distribution (HOD) models that provide an estimate of halo masses, $M_{\rm h} \sim (1 - 20) \times 10^{11}\,M_{\odot}$. Our $M_{\rm h}$ estimates agree with those obtained by previous clustering studies in a UV-magnitude versus $M_{\rm h}$ plane and allow us to calculate stellar-to-halo mass ratios (SHMRs) of LBGs. By comparison with the $z \sim 0$ SHMR, we identify evolution of the SHMR from $z \sim 0$ to $z \sim 4$ and from $z \sim 4$ to $z \sim 7$ at the >98% confidence levels. The SHMR decreases by a factor of ∼2 from $z \sim 0$ to 4 and increases by a factor of ∼4 from $z \sim 4$ to 7 at the dark matter halo mass of $M_{\rm h} \sim 10^{11}\,M_{\odot}$. We compare our SHMRs with results of a hydrodynamic simulation and a semianalytic model and find that these theoretical studies do not predict the SHMR increase from $z \sim 4$ to 7. We obtain the baryon conversion efficiency (BCE) of LBGs at $z \sim 4$ and find that the BCE increases with increasing dark matter halo mass. Finally, we compare our clustering+HOD estimates with results from abundance matching techniques and conclude that the $M_{\rm h}$ estimates of the clustering+HOD analyses agree with those of the simple abundance matching within a factor of 3, and that the agreement improves when using more sophisticated abundance matching techniques that include subhalos, incompleteness, and/or evolution in the star formation and stellar mass functions.

Key words: galaxies: evolution – galaxies: formation – galaxies: high-redshift

Supporting material: machine-readable table

1. INTRODUCTION

Dark matter halos play an important role in galaxy formation and evolution in the framework of Lambda cold dark matter (ΛCDM) structure formation models. Such halos can regulate processes such as gas cooling necessary for star formation. Gas cooling is efficient in halos with masses of 10^{10}–10^{13} $M_{\odot}$, where the gas cooling timescale is shorter than the gas infall timescale (Rees & Ostriker 1977; Silk & Wyse 1993; Sutherland & Dopita 1993). In low- and high-mass halos, feedback from supernovae (SNe), radiation pressure, and active galactic nuclei (AGNs) are thought to suppress star formation by thermal and kinetic energy input (e.g., Murray et al. 2005; Dekel et al. 2009; Kereš et al. 2009; Harikane et al. 2014). The connection between galaxies and their dark matter halos is essential for understanding galaxy formation, and specifically the stellar-to-halo mass ratio (SHMR), which is defined as the ratio of a galaxy's stellar mass to its halo mass, is one of the key quantities. The SHMR comprises the integrated efficiency of the past stellar mass assembly (i.e., star formation and mergers). The SHMR has been theoretically investigated with the help of hydrodynamic simulations or semianalytic models (e.g., Birrer et al. 2014; Hopkins et al. 2014; Okamoto et al. 2014; Thompson et al. 2014; Mitchell et al. 2015; Somerville et al. 2015). From observational studies, the SHMR is measured by analyses of galaxy clustering, weak lensing, satellite kinematics, and rotation curves at low redshift (e.g., Mandelbaum et al. 2006; More et al. 2011; Leauthaud et al. 2012; Coupon et al. 2015; Hudson et al. 2015; Rodríguez-Puebla et al. 2015; Shan et al. 2015; Skibba et al. 2015; Sofue 2015). These low-redshift studies find an SHMR with a peak at a dark matter halo mass of $M_{\rm h} \sim 10^{12}\,M_{\odot}$, independent of redshift, and referred to as a pivot halo mass. Leauthaud et al. (2012) claim a redshift evolution of SHMRs (and pivot halo masses) from $z \sim 0$ to $z \sim 1$. While some studies estimate the SHMR with clustering analysis at $z > 1$ (e.g., Foucaud et al. 2010; Durkalec et al. 2015; Hatfield et al. 2015; McCracken et al. 2015; Ishikawa et al. 2016), it is difficult to investigate the evolution of SHMR at these high redshifts due to poor statistics based on small galaxy samples available to date (see Hatfield et al. 2015; McCracken et al. 2015).

The abundance matching technique is another indirect probe of the SHMR. The abundance matching technique connects galaxies to their host dark matter halos by matching the cumulative stellar mass function (or the cumulative luminosity

function) and the cumulative halo mass function. Because this technique only requires one-point statistics that are easily measured, many recent studies apply this method from low-redshift to high-redshift galaxies (Behroozi et al. 2013a; Moster et al. 2013; Finkelstein et al. 2015; Mashian et al. 2015; Saito et al. 2015; Trac et al. 2015). Behroozi et al. (2013a) investigate the SHMR with abundance matching by using stellar mass functions, as well as specific star formation rates and cosmic star formation rate densities; they find that the SHMR evolves from $z = 0$ to $z = 8$. While abundance matching is a useful and less expensive method to connect galaxies to their dark matter halos, there are two major systematic uncertainties with respect to the application to high-redshift galaxies. One uncertainty is the star formation duty cycle (DC), which is defined as the probability of a halo of given mass to host an observable star-forming galaxy. Most abundance matching studies of $z \gtrsim 4$ Lyman break galaxies (LBGs) use the UV luminosity function, assuming that their star formation (i.e., UV-bright phase) DC is unity (see Behroozi et al. 2013a). However, star formation activity can be episodic. Moreover, populations of passive and dusty star-forming galaxies are expected to exist that may be missed in LBG samples. In fact, Lee et al. (2009) claim that the DC is ~0.3 at $z \sim 4$, and Ouchi et al. (2001) indicate a halo-mass-dependent DC based on clustering analysis. The other uncertainty, with respect to abundance matching, is the subhalo–galaxy relation. While the majority of abundance matching studies include subhalos (subhalo abundance matching; e.g., Behroozi et al. 2013a; Moster et al. 2013; Finkelstein et al. 2015; Mashian et al. 2015), the subhalo–galaxy relation is poorly constrained. For example, it is unclear which subhalo property best correlates with the stellar mass (or luminosity; Reddick et al. 2013; Guo et al. 2015). Preferably, one needs information independent from abundance to understand these systematics. Because lensing analysis is not feasible for galaxies at $z \gtrsim 2$ due to the limited number of background galaxies and their lower image quality, clustering analysis is a promising technique to test the abundance matching results and to extend our understanding of the connection between galaxies and dark matter halos to high redshift.

The clustering analysis of the high-redshift galaxies has been conducted with large-survey data. Ouchi et al. (2001, 2004b, 2005) obtained wide-area data taken with the Subaru deep survey and studied the clustering of LBGs at $z \sim 4$ and 5. Also Hildebrandt et al. (2009) estimated the angular correlation functions (ACFs) of LBGs at $z \sim 3$–5 with high accuracy using the Canada–France–Hawaii Telescope Legacy Survey (CFHTLS) data. With the LBT Boötes field survey data, Bian et al. (2013) studied the clustering properties of LBGs at $z \sim 3$. Recently, the deep data of the *Hubble Space Telescope* (*HST*) legacy survey allowed us to study LBGs at $z \sim 7$ (Barone-Nugent et al. 2014). Furthermore, Ishikawa et al. (2015) investigated the clustering properties of $z \sim 2$ star-forming galaxies using the wide-area data taken by the United Kingdom Infra-Red Telescope (UKIRT), Subaru telescope, and CFHT.

Recently a wide-field mosaic CCD camera, Hyper Suprime-Cam (HSC; Miyazaki et al. 2012), has been installed at the prime focus of the Subaru telescope (Iye et al. 2004). HSC has a field of view of 1.75 $\deg^2$ with a high sensitivity accomplished with the Subaru 8 m primary mirror. An HSC legacy survey under the Subaru Strategic Program (SSP; PI: S. Miyazaki) has been allocated 300 nights over 5 yr, and has been ongoing since 2014 March.[11] The HSC SSP has three survey layers of Wide, Deep, and Ultradeep that will cover the sky areas of 1400, 27, and 3.5 $\deg^2$ with the 5σ point-source limiting magnitudes of $r \simeq 26$ mag, $r \simeq 27$ mag, and $r \simeq 28$ mag, respectively. It is expected that full HSC SSP data sets will provide us with $\sim 2 \times 10^7$ LBGs at $z \gtrsim 4$, which is ~400 times larger than current samples identified in the deep fields of the CFHTLS (Hildebrandt et al. 2009) and allows us to investigate statistical properties of LBGs down to $\sim 0.1L^*$. Complementing these HSC SSP efforts, recent deep *HST* observations with Advanced Camera for Surveys (ACS) and Wide Field Camera 3 (WFC3) provide samples of $>10^4$ LBGs whose luminosities reach below $\sim 0.1L^*$ (e.g., Bouwens et al. 2015; Ishigaki et al. 2015). In this study, we use the unique combined data sets of Subaru/HSC and *Hubble*/ACS +WFC3 to investigate the galaxy–dark matter connection using LBGs over a wide luminosity range and investigate SHMRs at $z \gtrsim 4$, for the first time, using clustering analyses.

This paper is organized as follows. We present the observational data sets of Subaru/HSC and *Hubble*/ACS +WFC3 in Section 2. We describe the photometry and sample selection of LBGs in Section 3. The clustering analysis is presented in Section 4. Sections 5 and 6 detail our results on the dark matter halo mass and SHMR, respectively. We discuss the implications of the SHMR evolution and differences between our results and those from abundance matching in Section 7. Section 8 summarizes our findings. Throughout this paper we use the following cosmological model: $\Omega_m = 0.3$, $\Omega_\Lambda = 0.7$, $\Omega_b = 0.045$, $H_0 = 70$ km s^{-1} Mpc^{-1}, and $\sigma_8 = 0.8$. We use r_{200}, which is the radius in which the mean enclosed density is 200 times higher than the mean cosmic density. To define the halo mass, we use M_{200}, which is the total mass enclosed in r_{200}. We assume a Chabrier (2003) initial mass function (IMF). All magnitudes are in the AB system (Oke & Gunn 1983).

2. OBSERVATIONAL DATA SETS

2.1. Hubble Data

We use 10 deep optical–near-IR imaging data sets of the *Hubble* Ultra Deep Field (HUDF), Great Observatories Origins Deep Survey (GOODS)-North-Deep, GOODS-North-Wide, GOODS-South-Deep, GOODS-South-Wide, Cosmic Assembly Near-infrared Deep Extragalactic Legacy Survey (CANDELS)-All-Wavelength Extended Groth Strip International Survey (AEGIS), CANDELS-Cosmological Evolution Survey (COSMOS), CANDELS-Ultra Deep Survey (UDS), *Hubble* Frontier Field (HFF)-Abell2744P, and HFF-MACS0416P that are taken with ACS and WFC3 on the *HST*. The total area of the *Hubble* data is ~600 arcmin^2. We mask regions that are contaminated by the halos of bright stars or diffraction spikes by visual inspection and measure limiting magnitudes in a 0.″35 diameter circular aperture with SDFRED (Yagi et al. 2002; Ouchi et al. 2004a), after homogenizations of the point-spread functions (PSFs; see Section 3.1.1 for more details). The typical FWHMs of the PSFs of ACS and WFC3 images are 0.″1 and 0.″2, respectively. The limiting magnitudes, PSF FWHMs, and effective areas of these images are summarized in Table 1.

[11] http://www.naoj.org/Projects/HSC/surveyplan.html

Table 1
Limiting Magnitudes of the *Hubble* Data

		5σ Limiting Magnitude										
		Hubble										CFHT/Subaru
Field	Area (arcmin^2)	B_{435}	V_{606}	i_{775}	I_{814}	z_{850}	Y_{105}	J_{125}	JH_{140}	H_{160}	coadd[a]	r
(1)	(2)	(3)	(4)	(5)	(6)	(7)	(8)	(9)	(10)	(11)	(12)	(13)
HUDF	3.7	30.0	30.5	30.1	29.3	29.6	30.2	29.9	29.8	29.9	30.6	…
GOODS-N-Deep	57.4	28.6	28.8	28.3	30.5	28.1	27.9	28.3	…	28.1	28.6	…
GOODS-N-Wide	58.2	28.6	28.7	28.2	29.9	28.0	27.7	27.6	…	27.5	28.1	…
GOODS-S-Deep	52.1	28.6	28.8	28.2	28.8	29.0	28.4	28.4	…	28.3	29.0	…
GOODS-S-Wide	30.4	28.6	28.8	28.2	28.4	28.0	27.7	27.8	…	27.6	28.3	…
CANDELS-AEGIS	174.9	…	28.3	…	27.8	…	…	27.6	…	27.7	28.0	28.1
CANDELS-COSMOS	122.0	…	28.3	…	28.0	…	…	27.6	…	27.6	27.9	27.9/27.7
CANDELS-UDS	129.3	…	28.2	…	28.2	…	…	27.5	…	27.6	27.9	28.2
HFF-Abell2744P	3.1	28.8	29.1	…	28.8	…	29.0	28.8	28.8	28.8	29.3	…
HFF-MACS0416P	3.8	28.6	28.9	…	28.8	…	29.3	29.1	29.1	29.0	29.5	…
PSF FWHM[b]	…	0.″12	0.″11	0.″10	0.″11	0.″11	0.″20	0.″20	0.″20	0.″20	0.″21	0.″8

Notes. Columns: (1) Field. (2) Effective area in arcmin^2. (3)–(12) Limiting magnitudes, which correspond to 5σ variations in the sky flux measured in a circular aperture of 0.″35 diameter in PSF-matched images. (13) Limiting magnitude defined by a 5σ sky noise in a 1.″0 diameter aperture. See Skelton et al. (2014) for limiting magnitudes in other bands.
[a] Coadd image of $Y_{105}J_{125}JH_{140}H_{160}$-bands.
[b] Mean PSF FWHM values.

2.1.1. HUDF

HUDF has the deepest ACS and WFC3 imaging data ever taken, from the combination of the three surveys, HUDF (Beckwith et al. 2006), HUDF09 (GO 11563; PI: G. Illingworth; e.g., Bouwens et al. 2010), and HUDF12 (GO 12498; PI: R. Ellis; e.g., Ellis et al. 2013; Koekemoer et al. 2013). We use the combined HUDF data set compiled by the eXtreme Deep Field (XDF) team[12] (Illingworth et al. 2013). The HUDF data consist of nine band images of $B_{435}V_{606}i_{775}I_{814}z_{850}Y_{105}J_{125}JH_{140}H_{160}$ and cover ∼4 arcmin^2 sky area. The 5σ limiting magnitudes are ∼30 mag over these nine bands.

2.1.2. GOODS-North and GOODS-South

We use the data sets of the GOODS-North and GOODS-South fields, available from the CANDELS and 3D-*HST* teams (Brammer et al. 2012; Skelton et al. 2014),[13,14] that are obtained by CANDELS (PIs: S. Faber and H. Ferguson; Grogin et al. 2011; Koekemoer et al. 2011). The GOODS fields are composed of deep and wide survey data whose 5σ limiting magnitudes are typically ∼28.5 and ∼27.5 mag, respectively. About half of the GOODS-North and GOODS-South fields are deep survey areas, while the remaining half of GOODS-North and one-quarter of the GOODS-South are wide survey areas. The GOODS-North and GOODS-South data are observed with bands of $B_{435}V_{606}i_{775}I_{814}z_{850}Y_{105}J_{125}H_{160}$ with effective areas of ∼120 and ∼90 arcmin^2, respectively.

2.1.3. CANDELS-AEGIS, CANDELS-COSMOS, and CANDELS-UDS

The largest area *Hubble* data sets in our study come from CANDELS-AEGIS, CANDELS-COSMOS, and CANDELS-UDS imaging data (Grogin et al. 2011; Koekemoer et al. 2011) available from the 3D-*HST* (Brammer et al. 2012; Skelton et al. 2014). These imaging regions are covered by ACS $V_{606}I_{814}$ and WFC3 $J_{125}H_{160}$ observations with the typical 5σ limiting magnitude of 27.5 mag. Ground-based optical images taken with the CFHT and Subaru telescope are also available for these fields. We use the CFHT *ugr*-band images of the CANDELS-AEGIS field, the CFHT *ugr*- and Subaru *BVr*-band images of the CANDELS-COSMOS field, and the CFHT *u*- and Subaru *BVr*-band images of the CANDELS-UDS field.

2.1.4. HFF-parallel

Our study also includes imaging data from HFF (PI J. Lotz; e.g., Ishigaki et al. 2015; Kawamata et al. 2015). These data are parallel-field observations of Abell 2744 and MACS 0416 galaxy clusters that are taken from the HFF team.[15] Because lensing effects such as magnification and survey volume distortion are negligibly weak in HFF parallel fields (see, e.g., Ishigaki et al. 2015), we regard these HFF parallel images as blank-field data. These two HFF parallel fields are observed with seven bands of $B_{435}V_{606}I_{814}Y_{105}J_{125}JH_{140}H_{160}$ over a total effective area of ∼7 arcmin^2. The typical 5σ limiting magnitude is 29.0 mag.

2.2. Subaru Data

Our study includes early data of the HSC SSP survey taken from 2014 March to November (S14A_0b). We use the HSC SSP Wide layer *griz* data of the *XMM* field (R.A. = $2^h17^m00^s$, decl. = −5°12′00″ [J2000]) and GAMA09h field (R. A. = $8^h47^m00^s$, decl. = 0°45′00″ [J2000]).[16] While the HSC data are ∼3–6 mag shallower than the *Hubble* data, the HSC data cover ∼90 times larger effective area: 8.3 and 6.9 deg^2 in *XMM* and GAMA09h, respectively. As a result, the HSC data can provide clustering measurements at the bright end. The HSC data are reduced by the HSC SSP collaboration

[12] https://archive.stsci.edu/prepds/xdf/
[13] http://candels.ucolick.org/
[14] http://3dhst.research.yale.edu/Home.html
[15] http://www.stsci.edu/hst/campaigns/frontier-fields/
[16] These are the central coordinates of the early HSC data that we use.

Table 2
Limiting Magnitudes of the Subaru/HSC Data

Field	Area (arcmin^2)	5σ Limiting Magnitude g	r	i	z
(1)	(2)	(3)	(4)	(5)	(6)
HSC-*XMM*	30,100	26.3	25.8	25.8	25.1
HSC-GAMA09h	24,800	26.3	25.7	25.3	25.0
PSF FWHM[a]	···	0.″82	0.″85	0.″62	0.″67

Note. Columns: (1) Field. (2) Effective area in arcmin^2. (3)–(6) Limiting magnitudes defined by a 5σ sky noise in a PSF-75%-flux-radius circular aperture in PSF-matched images.
[a] Mean PSF FWHM values.

with hscPipe (version 3.4.1), which is the HSC data reduction pipeline based on the Large Synoptic Survey Telescope (LSST) software pipeline (Ivezic et al. 2008; Axelrod et al. 2010). The HSC data reduction pipeline performs CCD-by-CCD reduction and calibration for astrometry, warping, coadding, and photometric zero-point measurements. The astrometric and photometric calibrations are based on the data of the Panoramic Survey Telescope and Rapid Response System (Pan-STARRS) 1 imaging survey (Schlafly et al. 2012; Tonry et al. 2012; Magnier et al. 2013). We mask imaging regions contaminated with diffraction spikes and halos of bright stars using the mask extension outputs from the HSC data reduction pipeline and information of bright stars from our source catalogs (Section 3.2.1) and the Sloan Digital Sky Survey DR12 (Alam et al. 2015).[17] We use the PSF outputs from the pipeline (Jee & Tyson 2011), and typical PSF FWHMs are 0.″6–0.″9. The 5σ limiting magnitudes measured with SDFRED are ∼25–26 mag (Table 2).

3. PHOTOMETRIC SAMPLES AND LBG SELECTIONS

3.1. Hubble Samples

3.1.1. Multiband Photometric Catalogs

We construct multiband source catalogs from the *Hubble* data. To measure object colors, we match the image PSFs to the WFC3 H_{160}-band images, whose typical FWHM of the PSF is ≃0.″2, the largest of the *Hubble* multiband images. We use SWarp (Bertin et al. 2002) to produce our detection images, which are the co-added data of Y_{105}-, J_{125}-, JH_{140}-, and H_{160}-band images. The 5σ limiting magnitudes of the detection images are typically ∼0.5 mag deeper than those of the single-band images (Table 1).

We perform source detection and photometry with SExtractor (Bertin & Arnouts 1996). We run SExtractor (version 2.8.6) in dual-image mode for each multiband image with its detection image having the parameter set as follows: DETECT_MINAREA = 6, DETECT_THRESH = 2.0, ANALYSIS_THRESH = 2.0, DEBLEND_NTHRESH = 32, and DEBLEND_MINCOUNT = 0.005. The total number of the objects detected is 130,655. We measure the object colors with MAG_APER magnitudes defined in a 0.″35 diameter circular aperture. We use the MAG_AUTO measurements of SExtractor for total magnitudes. In the CANDELS-AEGIS, CANDELS-COSMOS, and CANDELS-UDS fields, we use the CFHT and Subaru imaging data to reduce low-z interlopers from high-z galaxy samples. Because we only need magnitude upper limits of high-z galaxy candidates for this purpose, we do not homogenize the PSFs of the CFHT and Subaru images. We obtain aperture magnitudes of SExtractor MAG_APER with a 1.″0 diameter circular aperture. If a source is not detected in either a *Hubble* or CFHT/Subaru band, we replace the source flux with the 1σ upper-limit flux.

[17] http://www.sdss.org/dr12/

3.1.2. LBG Selection

We select LBGs from our source catalogs using color information. From the HUDF, GOODS-North, and GOODS-South source catalogs, we select LBGs at $z \sim 4$, 5, 6, and 7 with the following LBG color criteria as given in Bouwens et al. (2015):

$z \sim 4$

$$B_{435} - V_{606} > 1, \quad (1)$$

$$i_{775} - J_{125} < 1, \quad (2)$$

$$B_{435} - V_{606} > 1.6(i_{775} - J_{125}) + 1, \quad (3)$$

$z \sim 5$

$$V_{606} - i_{775} > 1.2, \quad (4)$$

$$z_{850} - H_{160} < 1.3, \quad (5)$$

$$V_{606} - i_{775} > 0.8(z_{850} - H_{160}) + 1.2, \quad (6)$$

$z \sim 6$

$$i_{775} - z_{850} > 1.0, \quad (7)$$

$$Y_{105} - H_{160} < 1.0, \quad (8)$$

$$i_{775} - z_{850} > 0.777(Y_{105} - H_{160}) + 1.0, \quad (9)$$

$z \sim 7$

$$z_{850} - Y_{105} > 0.7, \quad (10)$$

$$J_{125} - H_{160} < 0.45, \quad (11)$$

$$z_{850} - Y_{105} > 0.8(J_{125} - H_{160}) + 0.7. \quad (12)$$

We select galaxies that have a Lyman break according to the criteria of Equations (1), (4), (7), and (10) and exclude intrinsically red galaxies by the additional constraints of Equations (2), (3), (5), (6), (8), (9), (11), and (12). Figure 1 presents these color selection criteria, together with all sources from the HUDF catalog. These LBG color selection criteria are extensively tested by simulations and used to study evolution of the UV luminosity functions (e.g., Bouwens et al. 2015).

In the five fields of CANDELS-AEGIS, CANDELS-COSMOS, CANDELS-UDS, HFF-Abell2744P, and HFF-MACS0416P, the number of available multibands is smaller than those in HUDF and GOODS. We use different color criteria and select LBGs at $z \sim 5$, 6, and 7–8 in these five fields (Bouwens et al. 2015) as follows:

$z \sim 5$

$$V_{606} - I_{814} > 1.3, \quad (13)$$

$$I_{814} - H_{160} < 1.25, \quad (14)$$

$$V_{606} - I_{814} > 0.72(I_{814} - H_{160}) + 1.3, \quad (15)$$

$z \sim 6$

$$I_{814} - J_{125} > 0.8, \quad (16)$$

$$J_{125} - H_{160} < 0.4, \quad (17)$$

$$I_{814} - J_{125} > 2(J_{125} - H_{160}) + 0.8, \quad (18)$$

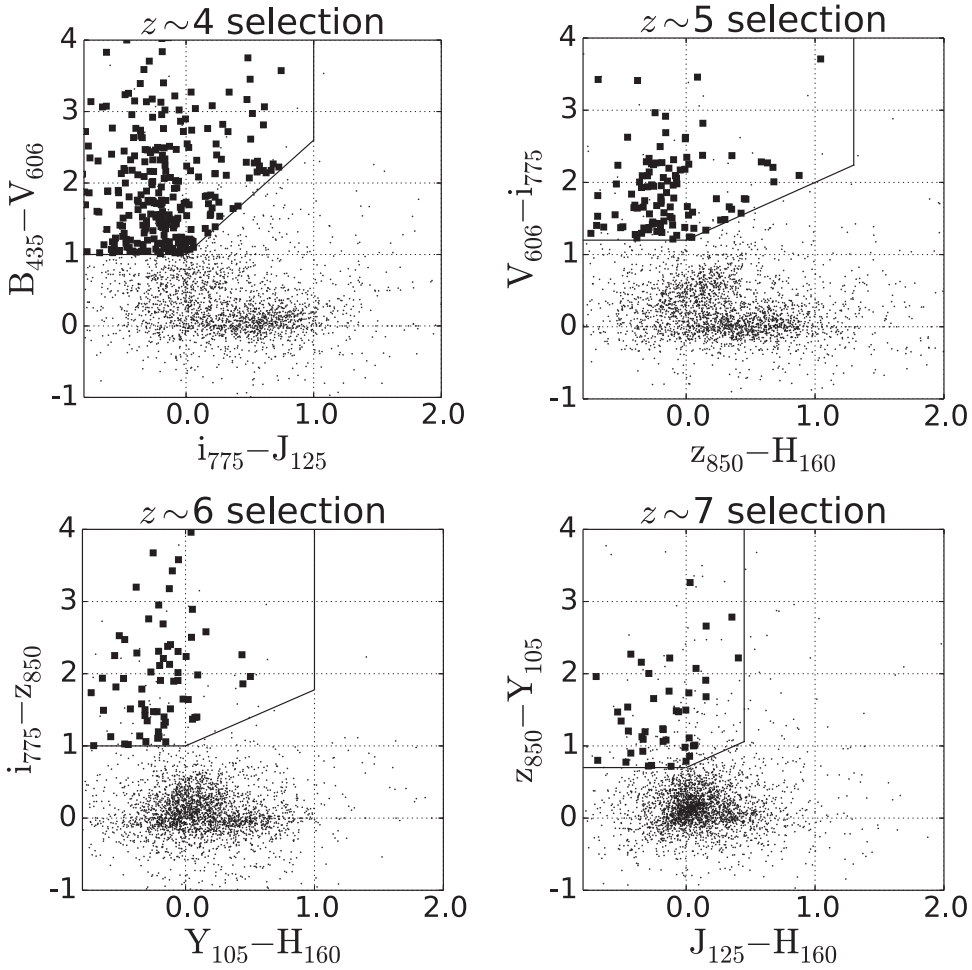

Figure 1. Two-color diagrams for selection of LBGs at $z\sim4$, 5, 6, and 7 from the *Hubble* data. The color selection criteria are indicated with solid lines. The black squares and dots denote colors of selected LBGs and other objects in the HUDF region, respectively. In addition to the color criteria indicated by the solid lines, we also enforce other criteria such as a nondetection in the images blueward of the Lyman break (see Section 3.1.2 for details).

$z\sim7-8$

$$I_{814}-J_{125}>2.2, \quad (19)$$

$$J_{125}-H_{160}<0.4, \quad (20)$$

$$I_{814}-J_{125}>2(J_{125}-H_{160})+2.2. \quad (21)$$

We select galaxies that have a Lyman break by the criteria given in Equations (13), (16), and (19) and exclude intrinsically red galaxies by the criteria of Equations (14), (15), (17), (18), (20), and (21).

In addition, we also adopt the following four criteria that are similar to those in Bouwens et al. (2015). First, to identify secure sources, we apply detection limits of $>5\sigma$ and $>5.5\sigma$ levels in the detection images in HUDF and the other fields, respectively. Since the HUDF data are deep and clean, the detection criterion of HUDF is more moderately loosened than the other fields. Second, for reducing foreground interlopers, we remove sources with continuum detected at wavelengths shortward of the Lyman breaks of the target LBGs. In all of the *Hubble* fields except CANDELS-AEGIS, CANDELS-COSMOS, and CANDELS-UDS, we apply the criterion of $<2\sigma$ nondetection in the B_{435} band for candidate LBGs at $z\sim5$ and $z\sim6$, if B_{435} data are available. Additionally, we require $<2\sigma$ nondetection in V_{606} band or $V_{606}-z_{850}>2.6$ for the $z\sim6$ LBG candidates. For the $z\sim7$ LBG candidates, we calculate an optical χ^2 value for each source with the $B_{435}V_{606}i_{775}$ flux measurements, if available, in the same manner as Bouwens et al. (2011). The optical χ^2 value is defined by $\chi^2_{\rm opt}=\Sigma_i {\rm SGN}(f_i)(f_i/\sigma_i)^2$, where f_i, σ_i, and ${\rm SGN}(f_i)$ are the flux in each band, its uncertainty, and its sign, respectively. We remove $z\sim7$ LBG candidates whose $\chi^2_{\rm opt}$ values are larger than 4. For the rest of the fields, CANDELS-AEGIS, CANDELS-COSMOS, and CANDELS-UDS, we calculate $\chi^2_{\rm opt}$ values using the ground-based data whose wavelengths are shorter than the redshifted Lyman break for the target LBGs at $z\sim5$, 6, and 7. We use a threshold value of 2, 3, or 4 that corresponds to the number of ground-based bands of <3, 3, or >4, respectively (Bouwens et al. 2015), and we remove LBG candidates whose $\chi^2_{\rm opt}$ value is larger than the threshold. Third, to isolate LBGs from foreground Galactic stars, the LBG candidates should have a SExtractor stellarity parameter, CLASS_STAR, less than 0.9 (Hildebrandt et al. 2009; Bouwens et al. 2015), if the candidates are 1 mag brighter than the detection limit. Finally, to avoid multiple identifications of a source satisfying two sets of selection criteria at different redshifts, we keep the source in a catalog of LBGs at a redshift higher than the other and remove the source from the low-z catalog. For example, if a source meets the criteria of Equations (4)–(6) and (7)–(9), the source is not included in the LBG catalog of $z\sim5$, but $z\sim6$. After adopting these

Table 3
Catalog of LBGs in the *Hubble* Data

Catalog ID	R.A. (J2000)	Decl. (J2000)	B_{435}	V_{606}	i_{775}	I_{814}	z_{850}	Y_{105}	J_{125}	JH_{140}	H_{160}	coadd[a]
z4_gdsd_7260	53.074684744	−27.880245679	29.4 ± 0.5	28.0 ± 0.1	27.7 ± 0.1	27.9 ± 0.1	28.0 ± 0.1	27.8 ± 0.1	28.1 ± 0.2	…	27.6 ± 0.1	28.2 ± 0.1
z4_gdsd_7269	53.075142909	−27.880051154	29.1 ± 0.4	27.6 ± 0.1	27.3 ± 0.1	27.4 ± 0.1	27.3 ± 0.0	27.7 ± 0.1	27.6 ± 0.1	…	27.8 ± 0.1	27.9 ± 0.1
z4_gdsd_7328	53.064744909	−27.87986999	29.4 ± 0.5	27.6 ± 0.1	27.3 ± 0.1	27.3 ± 0.1	27.3 ± 0.0	27.4 ± 0.1	27.4 ± 0.1	…	27.7 ± 0.1	28.6 ± 0.2
z4_gdsd_7433	53.065422101	−27.879309789	<30.3	29.4 ± 0.4	28.2 ± 0.2	28.2 ± 0.1	28.6 ± 0.2	28.5 ± 0.2	28.1 ± 0.2	…	28.0 ± 0.2	28.9 ± 0.2

Note. All magnitudes listed are measured in $0\farcs35$ diameter circular apertures. Upper limits are 1σ.
[a] Coadd image of $Y_{105}J_{125}JH_{140}H_{160}$ bands.

(This table is available in its entirety in machine-readable form.)

Table 4
Number of LBGs for Our Analysis

Field (1)	Area (arcmin^2) (2)	5σ Depth (3)	$z\sim4$ (4)	$z\sim5$ (5)	$z\sim6$ (6)	$z\sim7$ (7)
HUDF	3.7	30.6	290 (348)	48 (130)	0 (86)	0 (50)
GOODS-N-Deep	57.4	28.6	1411 (1655)	431 (630)	43 (136)	81 (113)
GOODS-N-Wide	58.2	28.1	788 (800)	193 (223)	63 (69)	27 (31)
GOODS-S-Deep	52.7	29.0	1139 (1872)	205 (696)	142 (311)	66 (203)
GOODS-S-Wide	30.4	28.3	461 (510)	92 (142)	28 (51)	13 (31)
CANDELS-AEGIS	174.9	28.0	…	304 (381)	73 (101)	0 (28)
CANDELS-COSMOS	122.0	27.9	…	314 (348)	76 (80)	0 (27)
CANDELS-UDS	129.3	27.9	…	268 (310)	54 (65)	0 (25)
HFF-Abell2744P	3.1	29.3	…	30 (37)	0 (26)	0 (7)
HFF-MACS0416P	3.8	29.5	…	56 (67)	0 (53)	0 (9)
HSC-*XMM*	30,100	25.1	…	451 (451)	…	…
HSC-GAMA09h	24,800	25.0	…	279 (279)	…	…
$N_{\rm total}(z)$			4089 (5185)	2671 (3694)	585 (978)	291 (524)
$N_{\rm total}$				7636 (10,381)		

Note. Columns: (1) Field. (2) Effective area in arcmin^2. (3) 5σ limiting magnitude in the coadd image. (3)–(7) Number of the LBGs for our analysis at each redshift that are brighter than the 5σ limiting magnitude in the rest-frame UV band whose central wavelength is nearest to rest-frame 1500 Å. The value in parentheses is the number of LBGs in the parent sample.

criteria, the estimated contamination fractions by foreground galaxies are estimated to be $f_{\rm c}\sim2\%$, 5%, 7%, and 9% for the $z\sim4$, 5, 6, and 7 LBG samples, respectively, based on the Monte Carlo simulations in Bouwens et al. (2015).

We construct a total sample of 5185, 2964, 978, and 524 LBGs at $z\sim4$, 5, 6, and 7, respectively, based on the *Hubble* data. Table 3 shows magnitudes of the LBGs. For conservative estimates of the clustering signals, we use the LBGs whose aperture magnitudes in the rest-frame UV band, $m_{\rm UV}^{\rm aper}$, are brighter than the 5σ limiting magnitudes. The rest-frame UV band is defined by the observed band whose central wavelength is nearest to the rest-frame wavelength of 1500 Å for the *Hubble* data and the Subaru data (Section 3.2). Table 4 summarizes the number of LBGs for each field. We compare our sample with the sample of Bouwens et al. (2015) and find that our sample is consistent with that of Bouwens et al. (2015). In the deep fields used in our comparison, more than ∼80% of the galaxies in our sample are included in the sample of Bouwens et al. (2015) at magnitudes brighter than the 10σ limiting magnitude. Similarly, more than ∼70% of the galaxies of the Bouwens et al. (2015) sample are included in our sample. The remaining 20%–30% of galaxies are located near the border of the color selection window and are missed due to photometric errors. We also compare the surface number densities of our LBGs with those of Bouwens et al. (2015) in Figure 2; we confirm that the surface number densities of our LBGs are consistent. The mean redshifts of the $z\sim4$, 5, 6, and 7 LBGs are $z_{\rm c}=3.8$, 4.9, 5.9, and 6.8, respectively, and the redshift distributions are the same as those shown in Figures 1 and 19 of Bouwens et al. (2015).

3.2. Subaru Samples

3.2.1. Multiband Photometric Catalogs

We make HSC source catalogs from the reduced images in the same manner as the *Hubble* source catalogs. First, we homogenize the PSFs of the HSC images to ∼0.″9 in FWHM by convolving images with a Gaussian, matching a PSF's 75%-flux circular radius that includes 75% of a total flux for a PSF profile source. We then run SExtractor (version 2.8.6) in dual-image mode to detect sources in the detection image, and to carry out photometry in the HSC images for `MAG_APER` in a circular aperture of the PSF's 75%-flux radius. The total magnitude is estimated from the aperture magnitude with an aperture correction. The aperture correction is estimated to be 0.31 mag under the assumption of the PSF profile. We use the parameter set of `DETECT_MINAREA` = 6, `DETECT_THRESH` = 1.5, `ANALYSIS_THRESH` = 1.5, `DEBLEND_NTHRESH` = 32, and `DEBLEND_MINCOUNT` = 0.005.

3.2.2. LBG Selection

We select LBGs at $z\sim5$ with the HSC data, because we can conduct secure selections with the g-band image. We apply color criteria similar to those of the CFHT study (Hildebrandt et al. 2009), which uses a photometric system almost identical to the one of our HSC data. The $z\sim5$ color selection criteria for the HSC sources are as follows:

$$r-i>1.2, \tag{22}$$

$$i-z<0.7, \tag{23}$$

$$r-i>1.5(i-z)+1.0. \tag{24}$$

We select galaxies that have a Lyman break by the criterion of Equation (22) and exclude intrinsically red galaxies by the criteria of Equations (23) and (24). These LBG color selection criteria are used for the study of clustering evolution (e.g., Hildebrandt et al. 2009).

In addition to the selection criteria above, we require sources to be detected at the $>5\sigma$ level in the z-band image and to be undetected at the $<2\sigma$ level in the g-band image. We also apply a criterion of SExtractor stellarity parameter, `CLASS_STAR`, of <0.9. We obtain 730 LBGs at $z\sim5$. The surface number densities of our HSC LBGs are presented in Figure 2, which agree with the previous results of Hildebrandt et al. (2009).

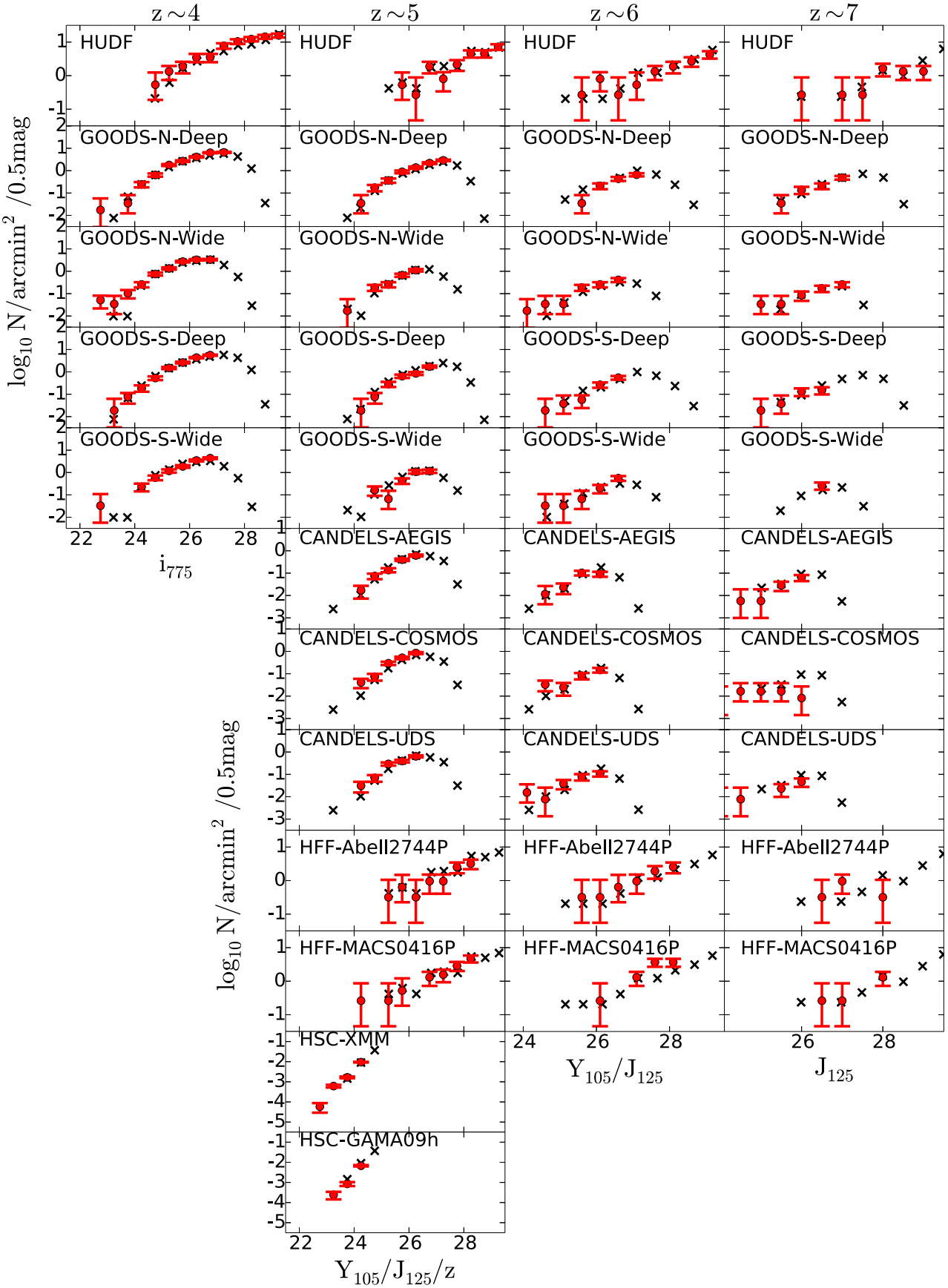

Figure 2. Surface number densities of LBGs at $z \sim 4$, 5, 6, and 7. The red circles represent the surface number densities of our LBGs, while the black crosses denote the surface number densities of the LBGs presented in the literature (Hildebrandt et al. 2009; Bouwens et al. 2015). The surface number densities of our LBGs are consistent with the previous results. We confirm that the errors of our surface number densities are comparable with Bouwens et al. (2015) in HUDF.

Table 5
Summary of the Clustering Measurements with the Power-law Model

z_c	$m_{\rm UV,th}^{\rm aper}$	$M_{\rm UV,th}$	$\langle M_{\rm UV}\rangle$	logSFR$_{\rm th}$	log $M_{*,\rm th}$	N	$n_{\rm g}$ (10^{-4} Mpc^{-3})	A_ω (arcsec$^{0.8}$)	r_0 (Mpc)	$b_{\rm g}$	χ^2_ν
(1)	(2)	(3)	(4)	(5)	(6)	(7)	(8)	(9)	(10)	(11)	(12)
3.8	27.2	−19.6	−20.2	0.97	9.1	1406	20.1 ± 3.5	1.2 ± 0.2	$5.7^{+0.4}_{-0.4}$	$2.9^{+0.2}_{-0.2}$	0.6
	27.6	−19.2	−19.8	0.77	8.9	2301	31.3 ± 4.9	1.0 ± 0.1	$5.1^{+0.3}_{-0.3}$	$2.6^{+0.1}_{-0.1}$	0.8
	28.2	−18.4	−19.3	0.35	8.4	2509	68.6 ± 11.7	0.8 ± 0.1	$4.4^{+0.2}_{-0.2}$	$2.4^{+0.1}_{-0.1}$	1.4
	29.2	−17.3	−18.4	−0.15	7.9	161	154.7 ± 53.8	0.4 ± 0.3	$3.0^{+1.0}_{-1.5}$	$1.7^{+0.5}_{-0.8}$	0.4
	29.8	−16.7	−17.9	−0.49	7.5	244	251.6 ± 65.6	0.2 ± 0.1	$2.2^{+0.8}_{-1.0}$	$1.2^{+0.4}_{-0.5}$	0.3
4.8	25.0	−21.7	−22.1	2.0	10.2	730	0.15 ± 0.10	8.8 ± 3.4	$14.5^{+2.9}_{-3.5}$	$8.2^{+1.5}_{-1.8}$	0.9
4.9	27.2	−19.9	−20.5	1.0	9.1	878	9.4 ± 1.3	2.0 ± 0.4	$6.4^{+0.7}_{-0.7}$	$4.0^{+0.4}_{-0.4}$	0.2
	27.6	−19.5	−20.0	0.84	8.9	1467	15.2 ± 1.7	1.4 ± 0.3	$5.2^{+0.5}_{-0.6}$	$3.3^{+0.3}_{-0.3}$	0.4
	28.0	−19.1	−19.8	0.67	8.7	623	22.0 ± 3.5	0.8 ± 0.3	$3.8^{+0.7}_{-0.8}$	$2.5^{+0.4}_{-0.5}$	0.3
	29.2	−17.9	−18.7	0.011	7.9	120	72.7 ± 30.4	1.2 ± 0.6	$4.9^{+1.1}_{-1.4}$	$3.1^{+0.6}_{-0.8}$	0.4
5.9	27.4	−20.0	−20.5	1.1	9.1	285	3.8 ± 0.6	2.7 ± 1.3	$6.4^{+1.5}_{-1.9}$	$4.7^{+1.0}_{-1.3}$	0.6
	28.4	−19.1	−19.3	0.55	8.6	278	13.4 ± 2.5	1.1 ± 0.7	$3.9^{+1.2}_{-1.6}$	$3.0^{+0.8}_{-1.2}$	0.6
6.8	28.2	−19.5	−19.9	0.75	8.8	113	7.0 ± 2.5	4.0 ± 1.2	$8.7^{+1.4}_{-1.6}$	$7.1^{+1.0}_{-1.2}$	0.6
	28.4	−19.3	−19.8	0.65	8.7	150	9.0 ± 2.2	1.8 ± 1.0	$5.5^{+1.6}_{-2.2}$	$4.7^{+1.2}_{-1.7}$	0.7

Note. Columns: (1) Mean redshift. (2) Threshold aperture magnitude in the rest-frame UV band. (3) Threshold absolute total magnitude in the rest-frame UV band. (4) Mean absolute total magnitude in the rest-frame UV band. (5) Threshold SFR in units of $M_\odot$ yr^{-1} derived from the threshold total magnitude, $M_{\rm UV,th}$. (6) Threshold stellar mass in units of $M_\odot$ derived from $M_{\rm UV,th}$ via Equations (58)–(60). (7) Number of galaxies in our subsample. (8) Number density of our subsample derived from a UV luminosity function of Bouwens et al. (2015). (9) Power-law amplitude (the power-law index is fixed to $\beta = 0.8$). (10) Spatial correlation length. (11) Galaxy–dark matter bias estimated by the power-law model. See column (6) in Table 6 for the best estimate from the HOD modeling. (12) Reduced χ^2 value.

More details of the data reduction and the LBG selection are presented in Y. Ono et al. (2016, in preparation).

4. CLUSTERING ANALYSIS

4.1. ACF

We derive the ACFs, $\omega(\theta)$, with our LBG samples. We calculate the observed ACFs, $\omega_{\rm obs}(\theta)$, using the estimator presented in Landy & Szalay (1993),

$$\omega_{\rm obs}(\theta) = \frac{\rm DD(\theta) - 2DR(\theta) + RR(\theta)}{\rm RR(\theta)}, \quad (25)$$

where DD(θ), DR(θ), and RR(θ) are numbers of galaxy–galaxy, galaxy–random, and random–random pairs normalized by the total number of pairs. We create a random sample composed of 10,000 (100,000) sources for each *Hubble* (Subaru) field with the geometrical shape the same as the observational data including the mask positions. The errors are estimated by the bootstrap technique of Ling et al. (1986), with 100 resamples replacing individual galaxies for each field. It is known that this bootstrap technique tends to overestimate the errors of the correlation function (Mo et al. 1992; Fisher et al. 1994). Although we cannot quantitatively evaluate this trend with our data, which are not large enough, the forthcoming data of the HSC survey will enable us to investigate this effect.

Due to the finite size of our survey fields, the observed ACF is underestimated by a constant value known as the integral constraint, IC (Groth & Peebles 1977). Including the correction for the number of objects in the sample, N (Peebles 1980), the true ACF is given by

$$\omega(\theta) = \omega_{\rm obs}(\theta) + {\rm IC} + \frac{1}{N}. \quad (26)$$

We estimate the integral constraint with

$${\rm IC} = \frac{\Sigma_i {\rm RR}(\theta_i)\omega_{\rm model}(\theta_i)}{\Sigma_i {\rm RR}(\theta_i)}, \quad (27)$$

where $\omega_{\rm model}(\theta)$ is the best-fit model ACF and i refers to the angular bin.

To test the dependence of the clustering strength on the luminosity of the galaxies, we make subsamples that are brighter than the threshold UV magnitudes, $m_{\rm UV,th}$, which are listed in Table 5. In each subsample, we obtain the best estimate of the ACF, which is the weighted mean of the ACFs of the different fields in an angular bin. Table 5 shows the numbers of LBGs in the subsamples. Note that the numbers of the faint-magnitude subsamples are smaller than those of bright-magnitude subsamples (e.g., $m_{\rm UV,th}^{\rm aper} = 29.2$–$29.8$ and 27.2–28.2). This is because the faint-magnitude subsamples are only composed of LBGs in very deep data covering a small field (e.g., HUDF). Using the UV luminosity functions of Bouwens et al. (2015), we calculate the number density of LBGs for each subsample and associated errors corrected for incompleteness. We estimate the cosmic variance in the number densities using the bias values obtained in Section 4.2, following the procedures in Somerville et al. (2004). We include the uncertainty from cosmic variance in our estimate of the error on the number density. The LBG number densities and the errors are presented in Table 5.

We fit the ACFs with a simple power-law model,

$$\omega(\theta) = A_\omega \theta^{-\beta}. \quad (28)$$

Because we obtain no meaningful constraints on β for most of the subsamples, we fix the value of β to 0.8, which is used in previous clustering analyses (e.g., Ouchi et al. 2001, 2004b, 2010; Foucaud et al. 2003, 2010). We use Equation (28) for $\omega_{\rm model}(\theta)$ to determine IC (Equation (27)) and obtain the best-fit A_ω values with Equation (26).

Contaminating sources in a galaxy sample reduce the value of A_ω. If contaminants have a homogeneous sky distribution, the true A_ω is underestimated by a factor of $(1-f_c)^2$, where f_c is a contamination fraction. Because contaminants are more or less clustered, a clustering amplitude multiplied by $1/(1-f_c)^2$ provides the upper limit of the value of A_ω,

$$A_\omega^{\max} = \frac{A_\omega}{(1-f_c)^2}. \quad (29)$$

The contamination fractions are $f_c \sim 2\%$, 5%, 7%, and 9% for the $z \sim 4$, 5, 6, and 7 LBG samples, respectively (Bouwens et al. 2015). The corresponding $1/(1-f_c)^2$ values are ∼1.04, 1.1, 1.2, and 1.2, which are significantly smaller than the statistical errors. Therefore, we do not apply these contamination corrections to our estimate of A_ω. Table 5 presents the best-fit A_ω values. In Figure 3, we plot ACFs of our subsamples with the best-fit power-law model.

4.2. Correlation Length and Bias

An ACF shows clustering properties of galaxies projected on the sky and depends on the combination of a galaxy redshift distribution and a galaxy spatial correlation function $\xi_g(r)$. The spatial correlation function is approximated by a single power law,

$$\xi_g(r) = \left(\frac{r}{r_0}\right)^{-\gamma}, \quad (30)$$

where r_0 is the correlation length. We calculate correlation lengths from the amplitudes of the ACFs using the Limber equation (Peebles 1980; Efstathiou et al. 1991),

$$A_\omega = C r_0^\gamma \frac{\int_0^\infty F(z) D_\theta(z)^{1-\gamma} N(z)^2 g(z) dz}{\left[\int_0^\infty N(z) dz\right]^2}, \quad (31)$$

$$g(z) = \frac{H_0}{c}(1+z)^2 \{1 + \Omega_m z + \Omega_\Lambda [(1+z)^{-2} - 1]\}^{1/2}, \quad (32)$$

$$C = \frac{\sqrt{\pi}\,\Gamma[(\gamma-1)/2]}{\Gamma(\gamma/2)}, \quad (33)$$

where $D_\theta(z)$ is the angular diameter distance and $N(z)$ is the redshift distribution of the sample. $F(z)$ describes the redshift dependence of $\xi(r)$. Assuming that the clustering pattern is fixed in comoving coordinates in the redshift range of our sample, we use the functional form $F(z) = [(1+z)/(1+z_c)]^{-(3+\epsilon)}$ for $\epsilon = -1.2$ (Roche & Eales 1999), where z_c is the average redshift of the sample LBGs (Section 3.1). The r_0 value does not significantly depend on ϵ over $-3 < \epsilon < 0$. The slope of the spatial correlation function, γ, is related to that of the ACF, β, by

$$\gamma = \beta + 1. \quad (34)$$

We adopt the redshift distribution of LBGs presented in Bouwens et al. (2015; left panel of Figure 1) and Y. Ono et al. (2016, in preparation) for our *Hubble* and Subaru samples, respectively. These redshift distributions include the photometric uncertainties based on the Monte Carlo simulations. Y. Ono et al. obtain the redshift distribution by placing artificial objects randomly in the real images using a method similar to the one in Bouwens et al. (2015). The object colors are calculated with redshifted model spectra (Bruzual & Charlot 2003) and the HSC filter response curves. We check the systematic errors on the halo mass estimates originating from the $N(z)$ uncertainties and find that the errors change the mass estimates negligibly, only by $\lesssim$0.05 dex, assuming the $\lesssim$15% systematic shift of $N(z)$ that is found in the spectroscopic results of Steidel et al. (1999).

We calculate the galaxy–dark matter bias b_g on the scale of $r = 8\ h^{-1}$Mpc, which is given by

$$b_g = \sqrt{\frac{\xi_g(r = 8\ h^{-1}\mathrm{Mpc})}{\xi_{DM}(r = 8\ h^{-1}\mathrm{Mpc}, z)}}, \quad (35)$$

where $\xi_{DM}(r, z)$ is the spatial correlation function of the underlying dark matter calculated with the linear dark matter power spectrum, $P_m(k, z)$, which is defined by

$$\xi_{DM}(r, z) = \int \frac{k^2 dk}{2\pi^2} \frac{\sin(kr)}{kr} P_m(k, z). \quad (36)$$

Table 5 presents the bias values thus obtained.

4.3. Halo Occupation Distribution (HOD) Model

To connect observed galaxies to their host dark matter halos, we use an HOD model, which is an analytic model of galaxy clustering (e.g., Seljak 2000; Berlind & Weinberg 2002; Cooray & Sheth 2002; Berlind et al. 2003; Kravtsov et al. 2004; Zheng et al. 2005). The HOD model is adopted not only to low-redshift galaxies (e.g., Zehavi et al. 2005; Zheng et al. 2007; van den Bosch et al. 2013; More et al. 2015) but also to high-redshift galaxies (e.g., Bullock et al. 2002; Hamana et al. 2004; Ouchi et al. 2005; Lee et al. 2006, 2009; Hildebrandt et al. 2007; Bian et al. 2013). The key assumption of our HOD model is that the number of galaxies, N, in a given dark matter halo depends only on the halo mass, M_h. We parameterize the mean number of galaxies in dark matter halos with a mass of M_h, $N(M_h)$, which is given by

$$N(M_h) = \mathrm{DC}(N_c(M_h) + N_s(M_h)), \quad (37)$$

where DC is the DC of LBG activity (see Section 1 for the definition). $N_c(M_h)$ and $N_s(M_h)$ are the mean number of central and satellite galaxies, respectively. Here the LBG activity for DC is defined by the properties of galaxies that are UV-bright star-forming galaxies selected as LBGs brighter than $m_{UV,th}$. We assume that DC does not depend on the halo mass in each subsample, because the present data are not large enough to investigate the mass dependence of DC that hides in the statistical errors. We adopt functional forms of $N_c(M_h)$ and $N_s(M_h)$ that are motivated by N-body simulations, smoothed particle hydrodynamic simulations, and semianalytic models for low-z galaxies and LBGs (e.g., Kravtsov et al. 2004; Zheng et al. 2005; Garel et al. 2015). $N_c(M_h)$ is approximated as a step function with a smooth transition,

$$N_c(M_h) = \frac{1}{2}\left[1 + \mathrm{erf}\left(\frac{\log M_h - \log M_{\min}}{\sigma_{\log M}}\right)\right], \quad (38)$$

where $\sigma_{\log M}$ is a transition width reflecting the scatter in the luminosity–halo mass relation. $M_{\min}$ is the mass scale at which 50% of halos host a central galaxy. Similarly, the mean number

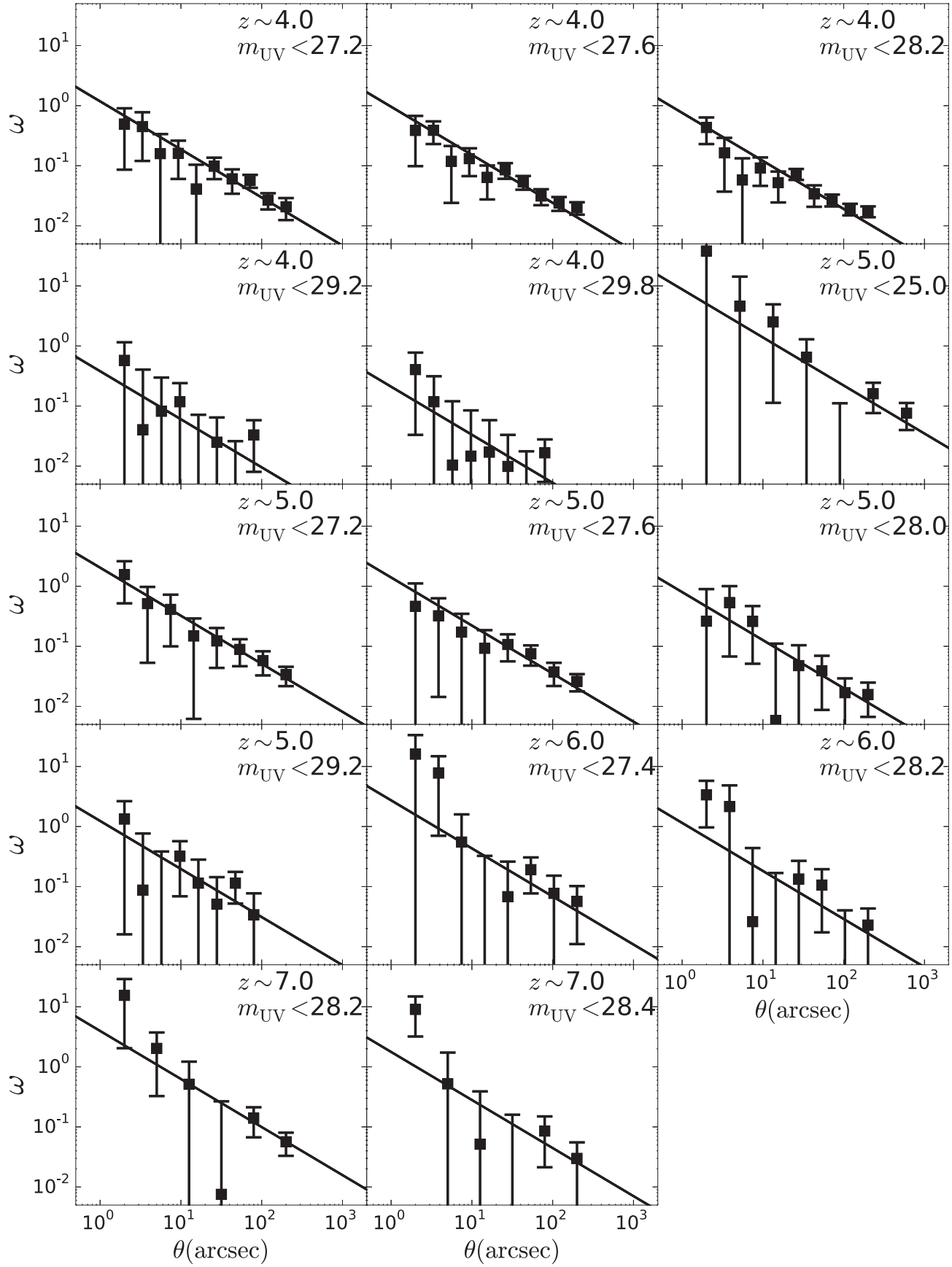

Figure 3. ACF of each subsample. The solid lines indicate the best-fit power-law function, $A_\omega\theta^{-\beta}$, where we fix $\beta = 0.8$. The redshift and threshold magnitude are denoted in the upper right corner of each panel.

of satellite galaxies, $N_s(M_h)$, follows a power law with a mass cut,

$$N_s(M_h) = N_c(M_h)\left(\frac{M_h - M_0}{M_1'}\right)^{\alpha}, \quad (39)$$

where M_0 is the cutoff mass and M_1' (α) is the amplitude (slope) of the power law.

We calculate galaxy number densities from the HOD model with

$$n_g(z) = \int_0^{\infty} dM_h \frac{dn}{dM_h}(M_h, z) N(M_h), \quad (40)$$

where $(dn/dM_h)(M_h, z)$ is the halo mass function. We use the halo mass function derived in Behroozi et al. (2013a), which is a modification of the Tinker et al. (2008) halo mass function for the high-redshift universe ($z > 2.5$) matching to the *Consuelo* simulation (McBride et al. 2009; see also Leauthaud et al. 2011; Behroozi et al. 2013b).[18] The difference between the Behroozi et al. (2013a) and Tinker et al. (2008) halo mass functions is ~10% in the number density of the $M_h \sim 10^{10}\,M_\odot$ dark matter halo at $z \sim 4$–7. If we use the original mass function of Tinker et al. (2008), we find that none of our conclusions are changed.

In our HOD model, $\xi_g(r)$ is computed from the galaxy power spectrum, $P_g(k)$, through the Fourier transformation,

$$\xi_g(r) = \frac{1}{2\pi^2}\int_0^{\infty} dk\; k^2 P_g(k)\frac{\sin kr}{kr}. \quad (41)$$

The galaxy power spectrum is described by

$$P_g(k) = P_g^{1h}(k) + P_g^{2h}(k), \quad (42)$$

where $P_g^{1h}(r)$ ($P_g^{2h}(r)$) is the one-halo (two-halo) term for pairs of galaxies in one (two different) halo(s).

The one-halo term consists of a central–satellite part $P_g^{cs}(k)$ and a satellite–satellite part $P_g^{ss}(k)$,

$$P_g^{1h}(k) = P_g^{cs}(k) + P_g^{ss}(k). \quad (43)$$

The quantities of $P_g^{cs}(k)$ and $P_g^{ss}(k)$ are given by

$$P_g^{cs}(k, z) = \frac{2}{n_g^2}\int dM_h \langle N_c N_s\rangle(M_h)\frac{dn}{dM_h}(M_h, z) u(k, M_h, z) \quad (44)$$

and

$$P_g^{ss}(k, z) = \frac{1}{n_g^2}\int dM_h \langle N_s(N_s - 1)\rangle(M_h)\frac{dn}{dM_h}(M_h, z) u^2(k, M_h, z), \quad (45)$$

where $u(k, M_h, z)$ is the Fourier transform of the dark matter halo density profile normalized by its mass (e.g., Cooray & Sheth 2002). Here we assume that satellite galaxies in halos trace the density profile of the dark matter halo by the NFW profile (Navarro et al. 1996, 1997), and we adopt the mass–concentration parameter relation by Bullock et al. (2001) with an appropriate correction (see Shimizu et al. 2003). If we assume the $z = 4$ mass–concentration parameter relation for the halo mass estimate of the $z \sim 7$ subsample, we find the negligible change of 0.05 dex in $\log M_{\rm min}$. The values of $\langle N_c N_s\rangle(M_h)$ and $\langle N_s(N_s - 1)\rangle(M_h)$ are the mean number of central–satellite and satellite–satellite galaxy pairs, respectively. If we assume the independence of central and satellite galaxies and a Poisson distribution of the satellite galaxy's distribution, these values are

$$\langle N_c N_s\rangle(M_h) = N_c(M_h) N_s(M_h), \quad (46)$$

$$\langle N_s(N_s - 1)\rangle(M_h) = N_s^2(M_h). \quad (47)$$

The two-halo term is expressed as

$$P_g^{2h}(k, z) = P_m(k, z)\left[\frac{1}{n_g}\int dM_h\; N(M_h)\frac{dn}{dM_h}(M, z) b_h(M_h, z) u(k, M_h, z)\right]^2, \quad (48)$$

where $b_h(M_h, z)$ is the halo bias factor (Tinker et al. 2010).

To compare with the observational results, we calculate the ACF from the galaxy power spectrum projecting on the redshift distribution using the Limber approximation (see, e.g., chapter 2 of Bartelmann & Schneider 2001),

$$\omega(\theta) = \int dz N^2(z)\left(\frac{dr}{dz}\right)^{-1}\int dk \frac{k}{2\pi} P_g(k, z) J_0[r(z)\theta k], \quad (49)$$

where $N(z)$ is the normalized redshift distribution of galaxies and $J_0(x)$ is the zeroth-order Bessel function of the first kind. Here we assume that $N_c(M)$ and $N_s(M)$ do not vary as a function of redshift within the redshift ranges of the subsamples. The quantity $r(z)$ is the radial comoving distance given by

$$r(z) = \frac{c}{H_0}\int_0^z \frac{dz}{\sqrt{\Omega_{m,0}(1+z)^3 + \Omega_{\Lambda,0}}}, \quad (50)$$

for a flat cosmology. The mean galaxy number density with a redshift distribution $N(z)$ is calculated by

$$n_g = \frac{\int dz [dV(r)/dz] N(z) n_g(z)}{\int dz [dV(r)/dz] N(z)}, \quad (51)$$

where $n_g(z)$ is defined by Equation (40) and $dV(r)/dz$ is the comoving volume element per unit solid angle,

$$\frac{dV(z)}{dz} = r^2(z)\frac{dr}{dz}. \quad (52)$$

5. DARK MATTER HALO MASS

5.1. HOD Model Fitting

We fit our HOD model to the ACF and the number density of each subsample, minimizing the χ^2 value,

$$\chi^2 = \sum_i \frac{[\omega_{\rm obs}(\theta_i) - \omega_{\rm model}(\theta_i)]^2}{\sigma_\omega^2(\theta_i)} + \frac{[\log n_g^{\rm obs} - \log n_g^{\rm model}]^2}{\sigma_{\log n_g}^2}. \quad (53)$$

[18] http://lss.phy.vanderbilt.edu/lasdamas/

Table 6
Summary of the Clustering Measurements with Our HOD Model

z_c (1)	$m_{\rm UV,th}^{\rm aper}$ (2)	$\log M_{\rm min}$ (3)	DC (4)	$\log M_1'$ (5)	$b_g^{\rm eff}$ (6)	$\log\langle M_{\rm h}\rangle$ (7)	χ^2_ν (8)
3.8	27.2	$11.42^{+0.07}_{-0.12}$	$0.50^{+0.17}_{-0.16}$	$(12.19^{+0.08}_{-0.15})$	$3.6^{+0.1}_{-0.2}$	$11.89^{+0.04}_{-0.07}$	0.9
	27.6	$11.39^{+0.05}_{-0.09}$	$0.99^{+0.01}_{-0.32}$	$12.35^{+0.20}_{-0.19}$	$3.5^{+0.1}_{-0.1}$	$11.80^{+0.04}_{-0.06}$	0.8
	28.2	$11.15^{+0.06}_{-0.13}$	$0.80^{+0.12}_{-0.29}$	$12.07^{+0.21}_{-0.28}$	$3.1^{+0.1}_{-0.1}$	$11.67^{+0.04}_{-0.06}$	1.1
	29.2	$10.78^{+0.18}_{-0.25}$	$0.95^{+0.03}_{-0.54}$	$(11.59^{+0.12}_{-0.35})$	$2.8^{+0.2}_{-0.2}$	$11.60^{+0.06}_{-0.07}$	0.8
	29.8	$10.55^{+0.14}_{-0.28}$	$0.28^{+0.33}_{-0.13}$	$(11.17^{+0.17}_{-0.33})$	$2.6^{+0.1}_{-0.1}$	$11.54^{+0.04}_{-0.05}$	1.3
4.8	25.0	$12.25^{+0.05}_{-0.14}$	0.60 (fix)	$(13.18^{+0.06}_{-0.18})$	$7.6^{+0.3}_{-0.7}$	$12.35^{+0.05}_{-0.13}$	1.6
4.9	27.2	$11.35^{+0.05}_{-0.19}$	0.60 (fix)	$(12.12^{+0.24}_{-0.17})$	$5.0^{+0.1}_{-0.7}$	$11.66^{+0.02}_{-0.23}$	0.3
	27.6	$11.22^{+0.06}_{-0.18}$	0.60 (fix)	$(11.96^{+0.08}_{-0.20})$	$4.7^{+0.2}_{-0.4}$	$11.56^{+0.06}_{-0.10}$	0.9
	28.0	$11.11^{+0.10}_{-0.18}$	0.60 (fix)	$(11.80^{+0.11}_{-0.20})$	$4.4^{+0.2}_{-0.3}$	$11.48^{+0.06}_{-0.10}$	1.8
	29.2	$10.78^{+0.18}_{-0.24}$	0.60 (fix)	$(11.46^{+0.20}_{-0.26})$	$3.8^{+0.3}_{-0.3}$	$11.31^{+0.10}_{-0.10}$	0.5
5.9	27.4	$11.30^{+0.10}_{-0.13}$	0.60 (fix)	$(12.06^{+0.12}_{-0.16})$	$6.3^{+0.4}_{-0.4}$	$11.53^{+0.08}_{-0.10}$	0.5
	28.4	$11.03^{+0.05}_{-0.18}$	0.60 (fix)	$(11.75^{+0.07}_{-0.22})$	$5.5^{+0.2}_{-0.4}$	$11.30^{+0.07}_{-0.08}$	1.4
6.8	28.2	$11.04^{+0.08}_{-0.22}$	0.60 (fix)	$(11.77^{+0.07}_{-0.28})$	$6.8^{+0.2}_{-0.8}$	$11.28^{+0.04}_{-0.18}$	0.9
	28.4	$10.99^{+0.06}_{-0.20}$	0.60 (fix)	$(11.69^{+0.07}_{-0.27})$	$6.3^{+0.4}_{-0.4}$	$11.18^{+0.09}_{-0.11}$	0.6

Note. Columns: (1) Mean redshift. (2) Threshold magnitude in the rest-frame UV band. (3) Best-fit value of $M_{\rm min}$ in units of $M_\odot$. (4) Star formation duty cycle. (5) Best-fit value of M_1' in units of $M_\odot$. The value in parentheses is derived from $\log M_{\rm min}$ via Equation (55). (6) Effective bias. (7) Mean halo mass in units of $M_\odot$. (8) Reduced χ^2 value.

We simply use the diagonal elements in the covariance matrix, in the same manner as Hamana et al. (2004) and Zheng et al. (2007), because the errors of our correlation functions are dominated by the Poisson errors due to the small number statistics. In fact, if we include off-diagonal elements in the covariance matrix, changes in the best-fit value and 1σ errors of $\log M_{\rm min}$ are small, $\sim$0.06 dex, which does not change our conclusions.

We constrain the parameters of our HOD model using the Markov Chain Monte Carlo (MCMC) parameter estimation technique. Our HOD model has a total of six parameters: DC, $M_{\rm min}$, $\sigma_{\log M}$, M_0, M_1', and α. However, it is difficult to constrain all six of these parameters with our data, whose statistical accuracies are not high. We thus fix $\sigma_{\log M} = 0.2$ and $\alpha = 1.0$, following results of previous studies (e.g., Kravtsov et al. 2004; Zheng et al. 2005; Conroy et al. 2006). To derive M_0 from M_1', we use the relation

$$\log M_0 = 0.76 \log M_1' + 2.3, \tag{54}$$

which is given by Conroy et al. (2006) at $z \sim 0$–5 based on their simulations.

Our HOD model with three parameters, DC, $M_{\rm min}$, M_1', is fitted to the subsamples of $z \sim 4$ LBGs with $m_{\rm UV,th} = 27.6$–28.2, whose measurements have moderately high signal-to-noise ratios. The best-fit parameters are summarized in Table 6.

Note that the rest of the $z \sim 4$ LBG subsamples with $m_{\rm UV,th} = 27.2$, 29.2, and 29.8 do not have statistical accuracies high enough to constrain M_1', which describes the small-scale clustering.[19] We thus adopt another relation:

$$\log M_1' = 1.18 \log M_{\rm min} - 1.28, \tag{55}$$

which is calibrated with the results of Martinez-Manso et al. (2015). We obtain the best-fit parameters, which are summarized in Table 6. In the left panels of Figure 4, we plot the ACFs with the best-fit HOD model curves. The models and the data agree well. The right panels of Figure 4 are error contours in our HOD model obtained from the MCMC run.

The $z \geqslant 5$ subsamples have statistical uncertainties even higher than the $z \sim 4$ subsamples. Here we calculate the mean DC value from the $z \sim 4$ subsample fitting results to be DC $= 0.6^{+0.2}_{-0.3}$. Assuming that DC does not evolve by redshift, we use DC $= 0.6$ in our model fitting for the $z \geqslant 5$ subsamples. We thus obtain the $M_{\rm min}$ estimates as summarized in Table 6. The errors of $M_{\rm min}$ include statistical uncertainties in the fitting with DC $= 0.6$ and uncertainties originating from the DC determination (DC $= 0.6^{+0.2}_{-0.3}$). Figures 5 and 6 are the same as Figure 4, but for the $z \geqslant 5$ subsamples. Because DC is fixed to DC $= 0.6$, the right panels of Figures 5 and 6 show the probability distributions of $M_{\rm min}$.

5.2. Dark Matter Halo Mass Estimates

From the best-fit HOD model parameters, we calculate the effective galaxy bias

$$b_{\rm g}^{\rm eff} = \frac{1}{n_{\rm g}} \int dM_{\rm h} \frac{dn}{dM_{\rm h}}(M_{\rm h}, z) N(M_{\rm h}) b_{\rm h}(M_{\rm h}, z) \tag{56}$$

and the mean dark matter halo mass of central and satellite galaxies

$$\langle M_{\rm h}\rangle = \frac{1}{n_{\rm g}} \int dM_{\rm h} \frac{dn}{dM_{\rm h}}(M_{\rm h}, z) N(M_{\rm h}) M_{\rm h}, \tag{57}$$

and we present the results in Table 6. Most of the effective biases estimated by Equation (56) are systematically larger than the biases estimated by Equation (35), probably because the effective bias with Equation (56) is the average bias including the satellite galaxies, the majority of which reside in the massive halos.

Figure 7 shows $\langle M_{\rm h}\rangle$ as a function of $\langle M_{\rm UV}\rangle$, which is the mean of the absolute UV magnitude of the LBG subsample. The dark matter halo masses from the *Hubble* data fall in the range of $\langle M_{\rm h}\rangle \sim (1-8) \times 10^{11}\ M_\odot$, while the one from the HSC data is at the massive regime of $\langle M_{\rm h}\rangle \sim 2 \times 10^{12}\ M_\odot$.

[19] M_1' is sensitive to the one-halo term (see Equation (39)).

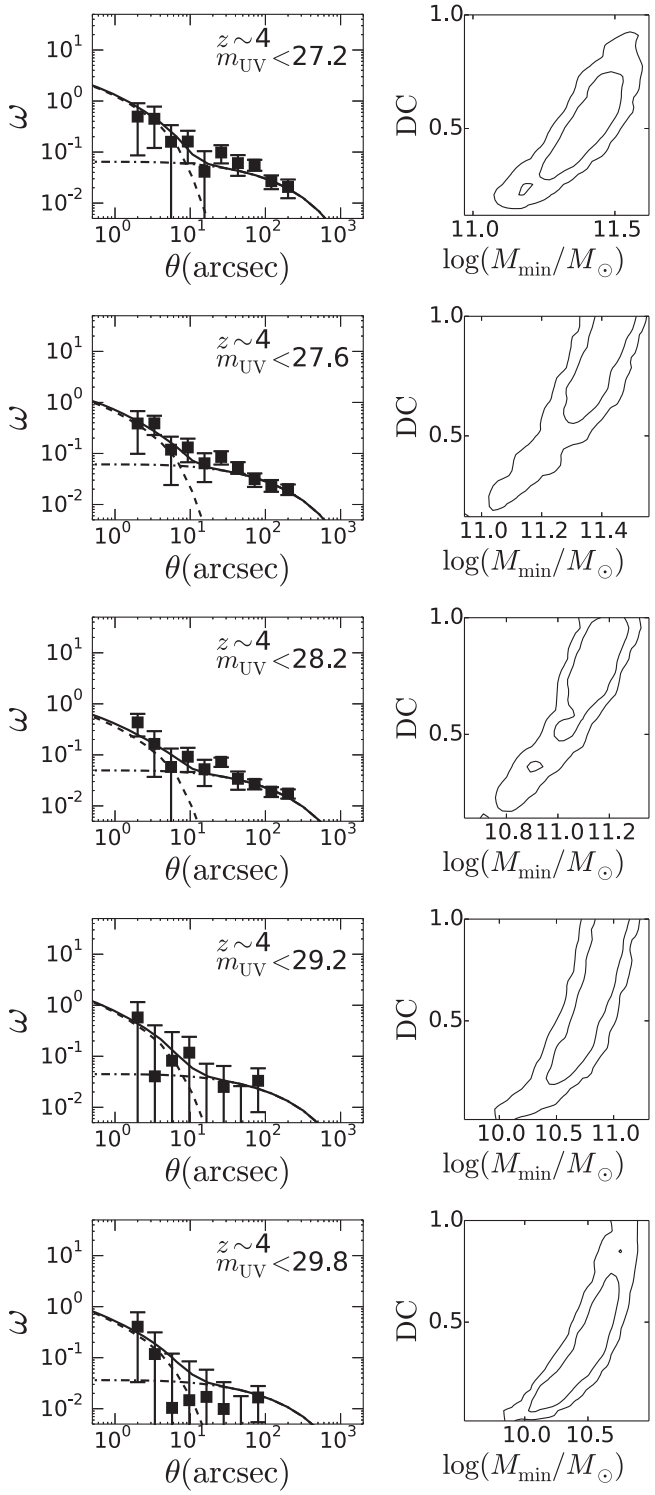

Figure 4. ACF and the best-fit HOD model at $z \sim 4$. Left panels: ACF with the prediction from our best-fit HOD model. The dashed and dot–dashed curves denote the one-halo and two-halo terms (Equations (43) and (48)), respectively. Right panels: error contour obtained from our MCMC run. The contours indicate the 68% and 95% confidence regions.

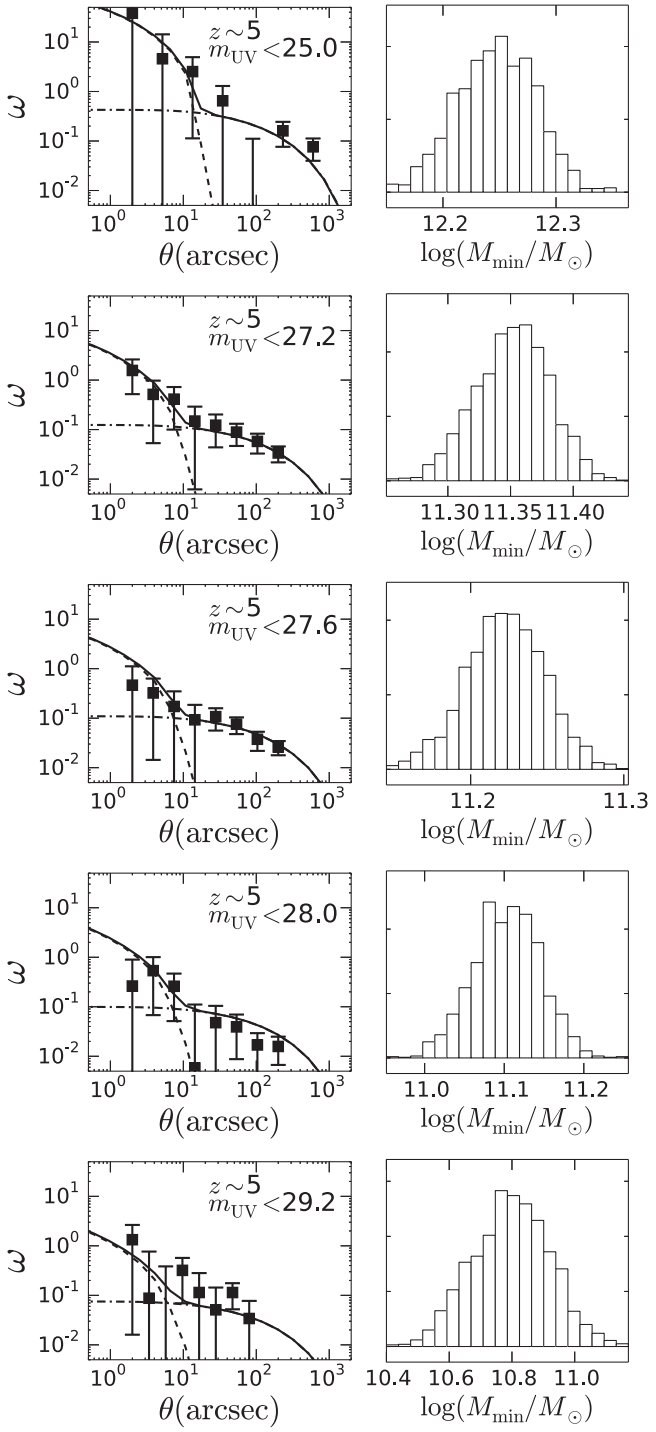

Figure 5. ACF and the best-fit HOD model at $z \sim 5$. Left panels: ACF with the prediction from our best-fit HOD model. The dashed and dot–dashed curves denote the one-halo and two-halo terms (Equations (43) and (48)), respectively. Right panels: probability distribution for $\log M_{\rm min}$ obtained from our MCMC run.

There is a trend of increasing dark matter halo mass with increasing UV luminosity at all redshifts. Our results suggest that more UV-luminous LBGs reside in more massive dark matter halos, and agree with the conclusions of previous high-z galaxy studies (Ouchi et al. 2001, 2004b, 2005; Foucaud et al. 2003; Adelberger et al. 2005; Lee et al. 2006; Bian et al. 2013; Barone-Nugent et al. 2014).

5.3. Comparison with Previous Clustering Studies

Figure 8 compares our results with previous clustering studies (Hamana et al. 2004; Ouchi et al. 2005; Lee et al. 2006; Hildebrandt et al. 2009; Barone-Nugent et al. 2014). Because

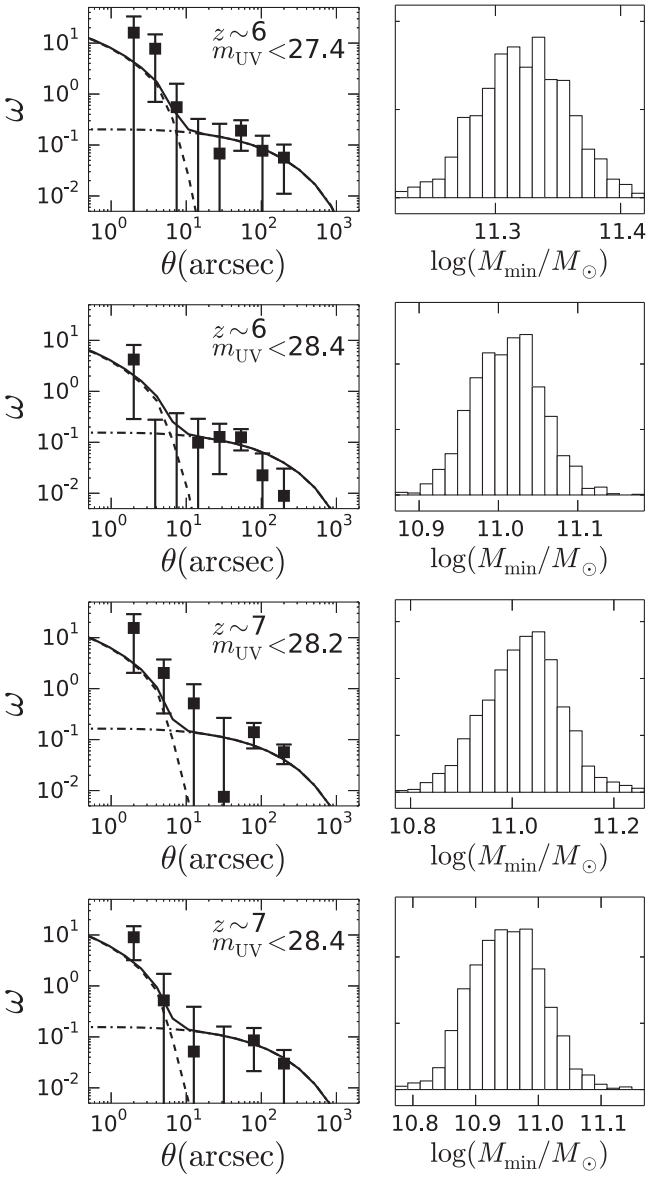

Figure 6. Same as Figure 5, but for $z \sim 6$ and 7.

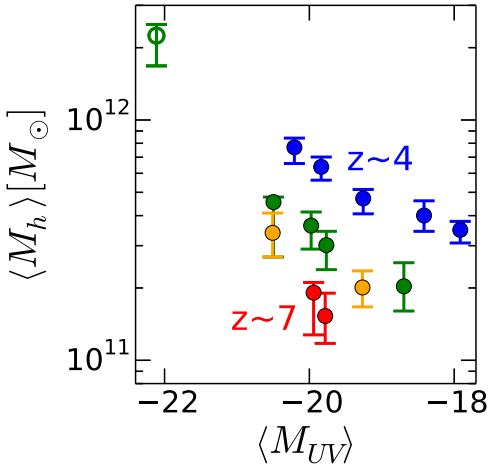

Figure 7. Mean dark matter halo mass as a function of mean absolute UV magnitude. The blue, green, orange, and red circles represent the mean dark matter halo mass of our *Hubble* subsample at $z \sim 4$, 5, 6, and 7, respectively. The open green circle denotes the mean dark matter halo mass of our subsample constructed from the HSC data.

most of the previous studies assume $\sigma_8 = 0.9$, which is different from our assumption ($\sigma_8 = 0.8$), we obtain our HOD model fitting results for our data with $\sigma_8 = 0.9$ for comparison. Similarly, the results of the previous studies are recalculated with the cosmological parameter sets with $\Omega_{\rm m} = 0.3$, $\Omega_\Lambda = 0.7$, $H_0 = 70$ km s^{-1} Mpc^{-1}, and $\sigma_8 = 0.9$. In this way, we conduct our comparisons using an equivalent set of cosmological parameters across all data sets. In Figure 8, we find that our $z \sim 4$ results are consistent with those of the previous studies within the uncertainties (see also Park et al. 2015). While the previous results at $z \sim 5$ are largely scattered, our $z \sim 5$ results are placed near the center of the distribution of the previous studies. At $z \sim 6$, our result agrees with that of Barone-Nugent et al. (2014). Over the full redshift range ($z \sim 4$–6) considered here, we confirm that our results are consistent with those of the previous studies. However, there is a 1σ–2σ difference between our results and those in Barone-Nugent et al. (2014) at $z \sim 7$. This difference may be simply explained by the measurement uncertainties or the difference of the LBG sample selections. As shown in Figure 8, we estimate the dark matter halo mass at $z \sim 6$–7 for the first time by the clustering analysis with the HOD model (see Barone-Nugent et al. 2014 by no HOD modeling). We also compare our results with the dark matter halo mass of $z \sim 3$ LBGs. Hildebrandt et al. (2009) estimate the mean dark matter halo mass of the $z \sim 3$ LBGs with $M_{\rm UV} < -20.0$ to be $(1.6 \pm 0.6) \times 10^{12}$ $M_\odot$, which is comparable to our result of $\langle M_{\rm UV} \rangle \sim -20$ at $z \sim 4$ (Figure 8; see also Adelberger et al. 2005; Lee et al. 2006; Hildebrandt et al. 2007; Bian et al. 2013).

6. SHMR

6.1. Stellar Mass Estimates

We estimate stellar masses M_* of our LBGs with the Chabrier (2003) IMF from UV magnitudes $M_{\rm UV}$, exploiting the star formation main sequence, a tight correlation between M_* and star formation rate (SFR) found at high z (e.g., Daddi et al. 2007; Speagle et al. 2014). Because LBGs at $z \gtrsim 4$ are generally very dust poor, SFR well correlates with $M_{\rm UV}$ (see also Steinhardt et al. 2014). Thus, $z \gtrsim 4$ LBGs have a correlation between $M_{\rm UV}$ and M_*. We use the $M_{\rm UV}$–M_* relations in Shibuya et al. (2015). These are the empirical $M_{\rm UV}$–M_* relations at $z = 0$–6 with photo-z galaxies in the 3D-*HST* catalog in Skelton et al. (2014), who carry out the SED fitting for the stellar mass with the Salpeter (1955) IMF. In order to convert our stellar-mass estimates of Salpeter (1955) to Chabrier (2003) IMFs, our final estimates are divided by a factor of 1.8. We thus estimate M_* from $M_{\rm UV}$ with the relations

$$\log M_* = -1.16 - 0.54 \times M_{\rm UV} \ (z \sim 4) \quad (58)$$

$$\log M_* = -2.28 - 0.59 \times M_{\rm UV} \ (z \sim 5) \quad (59)$$

$$\log M_* = -2.45 - 0.59 \times M_{\rm UV} \ (z \sim 6, 7). \quad (60)$$

Because Shibuya et al. (2015) show the $M_{\rm UV}$–M_* relations in the redshift ranges of $z = 3$–4, 4–5, and 5–6, we interpolate the relations in Shibuya et al. (2015) by redshift to derive Equations (58) and (59) for $z \sim 4$ and 5 LBGs, respectively. For $z \sim 6$ and 7 LBGs, we use the $M_{\rm UV}$–M_* relation of $z \sim 5$–6

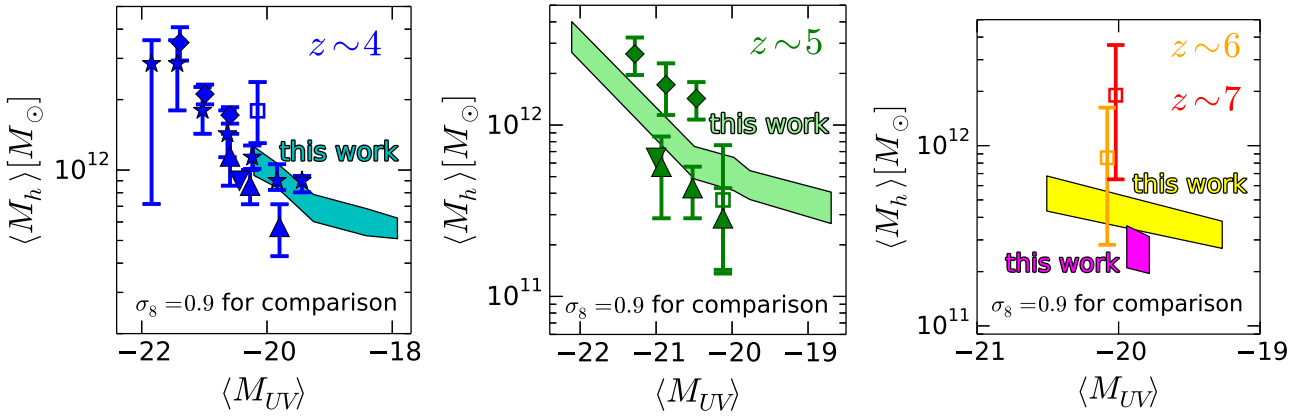

Figure 8. Comparison with previous clustering studies under the same cosmology, $\sigma_8 = 0.9$. Our results are recalculated with $\sigma_8 = 0.9$. Left panel: comparison at $z \sim 4$. The cyan shaded region represents the mean dark matter halo mass of our subsample at $z \sim 4$. The blue symbols represent the results of the previous studies. We plot the results of Hamana et al. (2004, downward triangle), Ouchi et al. (2005, stars), Lee et al. (2006, upward triangles), and Hildebrandt et al. (2009, diamonds). The downward triangle has no error bar, because Hamana et al. (2004) do not provide errors of the mean dark matter halo mass. We also show the results of Barone-Nugent et al. (2014) as a blue open square, who use the simple power-law model. We compile the results of Barone-Nugent et al. (2014) in the cosmology of $\Omega_m = 0.3$, $\Omega_\Lambda = 0.7$, $H_0 = 70$ km s^{-1} Mpc^{-1}, and $\sigma_8 = 0.9$. Center panel: comparison at $z \sim 5$. The light green shaded region represents the mean dark matter halo mass of our subsample at $z \sim 5$. The green symbols represent the results of the previous studies of Hamana et al. (2004, downward triangle), Lee et al. (2006, upward triangles), Hildebrandt et al. (2009, diamonds), and Barone-Nugent et al. (2004, open square). Right panel: comparison at $z \sim 6$, 7. The yellow and magenta shaded regions represent the mean dark matter halo masses of our subsample at $z \sim 6$, and 7, respectively. The orange and red open squares represent the results of Barone-Nugent et al. (2014) at $z \sim 6$, and 7, respectively.

given in Shibuya et al. (2015). If we extrapolate the $M_{\rm UV}$–M_* relation to $z \sim 6$ and 7, the derived stellar mass at $M_{\rm UV} = -20$ becomes larger by 0.1 dex at $z \sim 6$ and by 0.3 dex at $z \sim 7$, which do not change our conclusions (Section 6.2). We also confirm that our conclusions do not change if we use the $M_{\rm UV}$–M_* relations of Song et al. (2015). Note that the error on the mean relation between M_* and $M_{\rm UV}$ is <0.01 dex in the stellar mass, while the dispersion is 0.5 dex (Shibuya et al. 2015). In Table 5, we present estimates of the stellar masses $M_{*,\rm th}$ that correspond to the threshold UV magnitudes, $M_{\rm UV,th}$, of the subsamples.

6.2. SHMRs and the Evolution

Figure 9 presents SHMRs of central galaxies for our LBG subsamples at $z \sim 4$, 5, 6, and 7. Hereafter we use $M_{*,\rm th}$ and $M_{\rm min}$ values for stellar masses M_* and halo masses $M_{\rm h}$, respectively, because these quantities define our subsamples in a self-consistent manner. The black curve in Figure 9 represents the SHMR function at $z \sim 0$, which is the same as the one of Behroozi et al. (2013a), but for our cosmological parameters and stellar-mass estimate assumptions (P. Behroozi 2015, private communication).

In Figure 9, the combination of the *Hubble* and HSC data covers the wide halo mass range of 6×10^{10}–$2 \times 10^{12}\,M_\odot$ at $z \sim 5$. The SHMR increases from $\sim 10^{-3}$ to $\sim 10^{-2}$, with $M_{\rm h}$ increasing from $\sim 6 \times 10^{10}$ to $\sim 2 \times 10^{12}\,M_\odot$ at $z \sim 5$. Similar positive correlations are found in the SHMR–$M_{\rm h}$ relations at $z \sim 4$ and 6, as well as $z \sim 0$. The SHMRs at $z \sim 7$ are consistent with the positive correlation. At low redshift ($z \lesssim 1$), this correlation is claimed in various studies (e.g., Leauthaud et al. 2012; Coupon et al. 2015). Our results newly show the positive correlations of SHMR–$M_{\rm h}$ near $M_{\rm h} \sim 10^{11}\,M_\odot$ at high redshift, $z \sim 4$–6.

At $z = 0$–7, the SHMR values at $M_{\rm h} \sim 10^{11}$ are obtained, which allows us to investigate the evolution of SHMRs. From $z \sim 0$ to $z \sim 4$, the SHMR decreases by a factor of ~2, from $\sim 2.7 \times 10^{-3}$ to $\sim 1.3 \times 10^{-3}$. In contrast, the SHMR increases

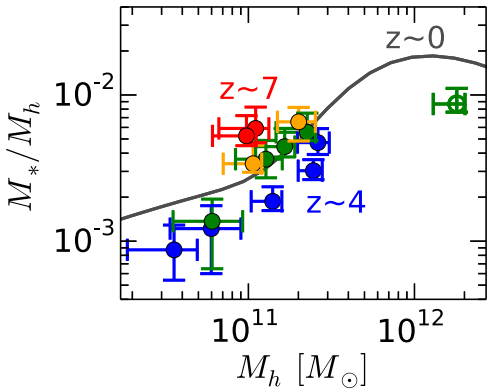

Figure 9. SHMR of central galaxies as a function of dark matter halo mass at $z \sim 4$, 5, 6, and 7. The blue, green, orange, and red circles represent the SHMR of our *Hubble* subsample at $z \sim 4$, 5, 6, and 7, respectively. The open green circle denotes the SHMR of our subsample constructed from the HSC data. The gray solid curve is the SHMR of Behroozi et al. (2013a) at $z \sim 0$, which is computed by P. Behroozi with the same cosmological parameters and halo mass definition as in our analysis.

by a factor of ~4, from $\sim 1.3 \times 10^{-3}$ at $z \sim 4$ to $\sim 5.3 \times 10^{-3}$ at $z \sim 7$. To quantify the evolution of the SHMR–$M_{\rm h}$ relation, we parameterize the $z \sim 0$ SHMR function of Behroozi et al. (2013a) with a pivot halo mass $M_{\rm pivot}$ and an SHMR amplitude at the pivot halo mass, SHMR$_{\rm pivot}$,

$$\begin{aligned}
&\log({\rm SHMR} - {\rm SHMR}_{\rm pivot}) \\
&= \log\left[\frac{M_*\,(M_{\rm h} - M_{\rm pivot})}{M_{\rm h} - M_{\rm pivot}}\right] \\
&= \log\left(\frac{\epsilon M_1}{M_{\rm h} - M_{\rm pivot}}\right) + f\left[\log\left(\frac{M_{\rm h} - M_{\rm pivot}}{M_1}\right)\right] - f(0),
\end{aligned} \tag{61}$$

$$f(x) = -\log(10^{\alpha x} + 1) + \delta\frac{\{\log[1 + \exp(x)]\}^\gamma}{1 + \exp(10^{-x})}, \tag{62}$$

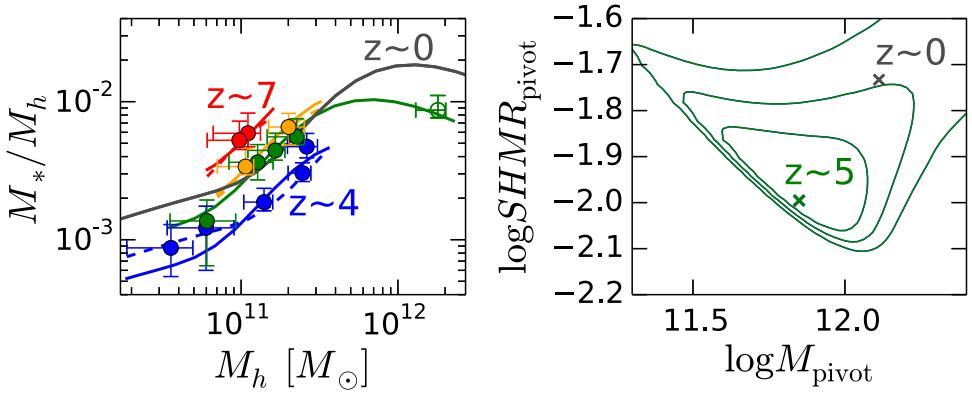

Figure 10. SHMR evolution. The left panel shows the results of our SHMR function fittings. The green curve represents the best-fit SHMR function at $z \sim 5$. We fit SHMR functions to our $z \sim 5$ SHMR–$M_{\rm h}$ data (green circles) by parametrizing the $z \sim 0$ SHMR function of Behroozi et al. (2013a) with a pivot mass, $M_{\rm pivot}$, and an SHMR amplitude at the pivot mass, $\rm SHMR_{pivot}$. The blue, orange, and red solid (dashed) curves describe the best-fit SHMR functions of $z \sim 4$, 6, and 7, respectively, in the $M_{\rm pivot}$-fixed ($\rm SHMR_{pivot}$-fixed) case. These curves are shown only in the range where measurements are available. The details of the fitting are presented in Section 6.2. In the right panel, the green contours represent the 1.0σ, 1.5σ, and 2.0σ confidence levels of $M_{\rm pivot}$ and $\rm SHMR_{pivot}$ at $z \sim 5$. The green cross in the contours corresponds to the best-fit values at $z \sim 5$. The gray cross shows the values of $M_{\rm pivot}$ and $\rm SHMR_{pivot}$ at $z \sim 0$ (Behroozi et al. 2013a).

where $\log \epsilon = -1.85$, $\log M_1 = 11.50$, $\alpha = -1.39$, $\delta = 3.76$, and $\gamma = 0.33$ at $z \sim 0$ (P. Behroozi 2015, private communication). We fit this parameterized SHMR function to our SHMR–$M_{\rm h}$ data of the $z \sim 4$–7 LBGs.

Removing the dependent results of our $m_{\rm UV,th}$ subsamples whose bright LBGs are repeatedly included in the subsamples, except for the HSC and some HUDF data, we only use the independent SHMR data in our fitting.

We use the subsamples of $m_{\rm UV}^{\rm aper} < 27.6$ mag and $m_{\rm UV}^{\rm aper} < 29.8$ mag ($m_{\rm UV}^{\rm aper} < 25.0$ mag, $m_{\rm UV}^{\rm aper} < 28.0$ mag, and $m_{\rm UV}^{\rm aper} < 29.2$ mag) for $z \sim 4$ ($z \sim 5$). Similarly, the $m_{\rm UV}^{\rm aper} < 28.4$ subsamples are fitted for $z \sim 6$, 7.

Because our $z \sim 5$ SHMR estimates are obtained in the wide halo mass range, which allows us to investigate the SHMR and $M_{\rm h}$ evolution simultaneously, we perform fitting to the $z \sim 5$ SHMR estimates with the SHMR function varying $M_{\rm pivot}$ and $\rm SHMR_{pivot}$. The best-fit function and the error contours are presented in the left and right panels of Figure 10, respectively. We compare these results with those at $z \sim 0$ obtained by Behroozi et al. (2013a). The left panel of Figure 10 indicates that the SHMRs of $z \sim 0$ and 5 are similar at $M_{\rm h} \sim 10^{11}\,M_\odot$, but different at $M_{\rm h} \sim 10^{12}\,M_\odot$. The massive end of our data makes a difference in the fitting result shown in the right panel of Figure 10.

Although the mass ranges of our SHMR data are limited, the SHMR results of $z \sim 4$ and 7 show large differences from those of $z \sim 0$ at $M_{\rm h} \sim 10^{11}\,M_\odot$. We quantify the differences by two extreme scenarios of $M_{\rm pivot}$-fixed and $\rm SHMR_{pivot}$-fixed cases that bracket the realistic scenario including both $M_{\rm pivot}$ and $\rm SHMR_{pivot}$ evolutions. Adopting the best-fit $M_{\rm pivot}$ or $\rm SHMR_{pivot}$ value at $z \sim 5$, we carry out the SHMR function fitting in these two cases. The left panel of Figure 10 presents the best-fit SHMR functions for $M_{\rm pivot}$-fixed and $\rm SHMR_{pivot}$-fixed cases with the solid and dashed lines, respectively. These two cases show very similar best-fit SHMR functions in the left panel of Figure 10, because the $M_{\rm h}$ ranges for the fitting are narrow and limited to $M_{\rm h} \sim 10^{11}\,M_\odot$. Moreover, the notable differences between $z \sim 0$, 4, and 7 curves are identified, suggesting the evolution of SHMR and/or $M_{\rm h}$ from $z \sim 0$ to $z \sim 4$ ($z \sim 0$–4) and from $z \sim 4$ to $z \sim 7$ ($z \sim 4$–7). In the $M_{\rm pivot}$-fixed ($\rm SHMR_{pivot}$-fixed) case, the differences of $z \sim 0$–4 and $z \sim 4$–7 are found at the 5.6σ and 3.1σ (3.3σ and 2.5σ) levels, respectively. In the calculations of these significance levels, we use the statistical error presented in Behroozi et al. (2010) as the error of the $z \sim 0$ SHMR, because Behroozi et al. (2013a) do not provide the statistical errors. Behroozi et al. (2010) use a similar data set to that of Behroozi et al. (2013a). We also investigate the $M_{*,\rm pivot}$-fixed case with varying $M_{\rm pivot}$, where $M_{*,\rm pivot}$ is the pivot *stellar* mass, not the pivot *halo* mass of $M_{\rm pivot}$. We find that the differences at the redshift ranges of $z \sim 0$–4 and $z \sim 4$–7 are 4.8σ and 2.7σ significance levels, respectively. In addition, we adopt the best-fit $M_{\rm pivot}$ or $\rm SHMR_{pivot}$ value of $z \sim 0$, instead of $z \sim 5$, and confirm that the arguments above are unchanged. In any cases of these scenarios, we find the SHMR evolutions at the redshift ranges of $z \sim 0$–4 and $z \sim 4$–7 at the >99% and >98% confidence levels, respectively. These SHMR evolutionary trends at $z \sim 0$–4 and $z \sim 4$–7 are identified, for the first time, based on the clustering analyses.

We examine whether these results are produced by systematic biases in our HOD model fitting, where we fixed some parameters and the analytic relations. First, we have assumed the fixed parameter of $\sigma_{\log M} = 0.2$ over $z = 4$–7 in Section 5, although it is known that $\sigma_{\log M}$ could vary with the redshift and the halo mass. According to the formulation of Behroozi et al. (2013a), $\sigma_{\log M}$ values of $z \sim 4$ and 7 galaxies of $M_{\rm h} \sim 10^{11}\,M_\odot$ are 0.3 and 0.5, respectively. Adopting $\sigma_{\log M} = 0.3$ for our $z \sim 4$ LBGs, we find negligible differences from the original $\sigma_{\log M} = 0.2$ results in the SHMR evolution from $z \sim 0$ to 4. We also estimate SHMR and $M_{\rm h}$ values with $\sigma_{\log M} = 0.5$ for our $z \sim 7$ LBGs. Although the estimated $M_{\rm h}$ values are larger than those of the original $\sigma_{\log M} = 0.2$ results by a factor of 1.5, the SHMR evolution from $z \sim 4$ to 7 is still found at the $\sim 2\sigma$ significance level. Second, we have adopted the analytic relations of Equations (54) and (55) to derive M_0 and M_1' in Section 5. Here we fit our ACFs with varying M_0 and M_1' as free parameters in the ranges of $9 < \log M_1' < 14$ and $8 < \log M_0 < 14$, respectively, to evaluate the impacts of the M_0 and M_1' values on our results. For all subsamples that we use in the SHMR evolution discussion, we find that the new $M_{\rm min}$ values from these fitting analyses agree with our best-estimate values (Table 6) within the uncertainties. For example, the subsample of $z \sim 4$ $m_{\rm UV} < 27.6$ mag gives the new $M_{\rm min}$ value of $\log M_{\rm min} = 11.4^{+0.1}_{-0.1}$, which is consistent with our best-

estimate value of $\log M_{\rm min} = 11.4^{+0.1}_{-0.1}$ (Table 6). Although some errors of the new $M_{\rm min}$ value are larger than those of the best-estimate value by a factor of ∼1.5, the SHMR evolution at $z \sim 0$–4 is still found at the $>3\sigma$ level due to the scatter of the new $M_{\rm min}$ value that separates the SHMRs of $z \sim 0$ and $z \sim 4$. The evolutions of the SHMR we find are more significant than the systematic biases.

We discuss systematic uncertainties in our SHMRs at $z \sim$ 4–7, by a comparison with that of Behroozi et al. (2013a) at $z \sim 0$. We derive the stellar masses assuming the Chabrier (2003) IMF and the Bruzual & Charlot (2003) stellar population synthesis models, which are also used in Behroozi et al. (2013a). Although the dust attenuation model in our analysis (Calzetti et al. 2000) is different from the one (Blanton & Roweis 2007) adopted by Behroozi et al. (2013a), this difference only changes the stellar mass estimate by 0.02 dex (Behroozi et al. 2010). The halo mass function in our analysis is the same as the one Behroozi et al. (2013a) use. The $z \sim 0$ SHMRs shown in our paper are recomputed by P. Behroozi with the same cosmological parameter set and halo mass definition as ours. Thus, the evolution of the SHMR at $z \sim 0$–4 is significant beyond these systematic uncertainties.

7. DISCUSSION

7.1. Interpretations of the SHMR Evolution

Figure 10 shows the redshift evolution of the SHMR at $z \sim$ 0–7 (Section 6.2). At the dark matter halo mass of $\sim 10^{11}\,M_\odot$, SHMRs decrease from $z \sim 7$ to 4 by 0.6 dex and increase from $z \sim 4$ to 0 by 0.3 dex. These two evolutionary trends of $\sim 10^{11}\,M_\odot$ dark matter halos suggest that the stellar-mass assembly is very (moderately) efficient at $z \gtrsim 7$ ($z \sim 0$–4), while it is inefficient at $z \sim 4$–7. There are three possible physical origins to explain the increase and decrease of SHMRs.

The first is the evolution of the gas cooling efficiency. The gas cooling efficiency is expected to be high if the number density or the chemical abundance of gas is high. At high redshift, the average density of the collapsed dark matter halos is very high due to the high cosmic matter density. Toward low redshift, the interstellar medium in galaxies becomes chemically enriched. If one tries to explain the SHMR evolution at $M_{\rm h} \sim 10^{11}\ M_\odot$ by the change of the gas cooling efficiency, the high SHMR at $z \sim 7$ would be reduced by the decreasing gas cooling efficiency due to the small number density at $z \sim 4$. In fact, Figure 7 indicates that low-redshift galaxies tend to have a high $\langle M_{\rm UV}\rangle$ (i.e., low SFR) for a given $\langle M_{\rm h}\rangle$. From $z \sim 4$ to $z \sim 0$, the SHMR may increase due to the increase of gas cooling efficiency that originated from the chemical enrichment.

The second is the evolution of feedback strengths. Because the mass of $\sim 10^{11}\,M_\odot$ falls in a moderately low mass regime, the SN and radiation pressure feedback are probably more important than AGN feedback (e.g., Okamoto et al. 2014). Typical LBGs at $z \gtrsim 7$ are very compact, having a half-light radius of $\lesssim$1 kpc (e.g., Shibuya et al. 2015). The gravitational potential at the dark matter halo center dominated by baryonic mass (Erb et al. 2006) is deeper at $z > 7$ than at $z \sim$ 4–7. At $z \sim$ 4–7, due to the moderately shallow gravitational potential, hot/warm gas is expelled from the center to the outer halo, and it takes time for the gas to come back to the central region by radiative cooling in the low-density regime of the outer halo. Although these dense and compact galaxies would allow the high SHMR values, the energy production rates corresponding to SFRs are also high (see Figure 8 and the discussion above). Thus, it is unclear whether feedback is responsible for the SHMR evolution at $z > 4$. Below $z \sim 4$, the decrease of specific SFRs (sSFRs; SFR divided by stellar mass) is accelerated toward low z (Whitaker et al. 2014). This fast decrease of sSFR and the increase of the galaxy half-light radius toward low z do not raise SHMRs at $z =$ 0–4. Thus, the feedback may not be major physical origins of the SHMR evolution of $z \sim$ 0–4.

The third is the evolution of merger rates and merger-induced star formation activities. In Section 6.2, we find that the SHMR positively correlates with $M_{\rm h}$ at $\sim 10^{11}\,M_\odot$ over $z \sim$ 0–7 (Figure 9). The shape of the SHMR–$M_{\rm h}$ function at $z \sim 0$ suggests that these positive correlations at $z \sim$ 0–7 continue to a halo mass range much lower than $M_{\rm h}$ at $\sim 10^{11}\,M_\odot$. If a merger is not associated with the star formation activity (i.e., dry merger), such a merger does not change the SHMR, but increases the halo mass. For example, if a galaxy with $\sim 10^{11}\,M_\odot$ forms by multiple mergers of $\sim 10^{10}\,M_\odot$ galaxies with no merger-induced star formation activity, the SHMR of the $\sim 10^{11}\,M_\odot$ galaxy is as low as those of the $\sim 10^{10}\,M_\odot$ galaxies. Under the condition of the positive correlation between SHMR and $M_{\rm h}$, this mechanism of mergers suppresses SHMRs. On the other hand, intensive star formation is followed by merger events. Such a merger-induced star formation would build up stellar masses and boost SHMRs. Thus, there are two effects of mergers: increasing and decreasing SHMRs. It is known that the merger rates decrease from high z to low z in simulations (Fakhouri et al. 2010). If one tries to explain the SHMR evolution at $\sim 10^{11}\,M_\odot$ by merger alone, the high SHMR raised by merger-induced star formation may be reduced by the decrease of the merger rate. At $z \sim$ 0–4, the merger-induced star formation should increase SHMRs faster than the merger suppression. Here we have discussed the three possible physical origins of the SHMR evolution at $z \sim$ 0–7. Although our observational results alone cannot determine what are the major physical origins, it is likely that the mixture of these effects gives the evolutionary trends of the SHMRs.

We discuss this SHMR evolution with the circular velocity,

$$V_{\rm cir} = \sqrt{\frac{GM_{\rm h}}{r_{200}}}. \quad (63)$$

Since the circular velocity is determined by the halo mass and radius, $V_{\rm cir}$ provides the condition for gas escaping from the halo by outflow. Figure 11 presents the SHMRs as a function of circular velocity for the $z \sim$ 4–7 LBGs. In Figure 11, the SHMRs of $z \sim 7$ are higher than those of $z \sim 4$ by 0.3 dex at $V_{\rm cir} \sim 160$ km s^{-1}. This increase is smaller than the 0.7 dex increase of the SHMR from $z \sim 4$ to 7 at $M_{\rm h} \sim 10^{11}\ M_\odot$ (Figure 10). Because the circular velocity for a given halo mass increases by redshift, the 0.7 dex SHMR evolution in the SHMR–$M_{\rm h}$ plane (Figure 10) is narrowed in the SHMR–$V_{\rm cir}$ plane (Figure 11). The small SHMR evolution in the SHMR–$V_{\rm cir}$ plane would indicate that the ($V_{\rm cir}$-dependent) gas outflow conditions are similar over the redshift range of $z \sim$ 4–7. In the SHMR–$V_{\rm cir}$ plane (Figure 11), there is a significant SHMR evolution of 0.5–1 dex at $z \sim$ 0–4 in contrast with the small SHMR evolution at $z \sim$ 4–7. This significant SHMR

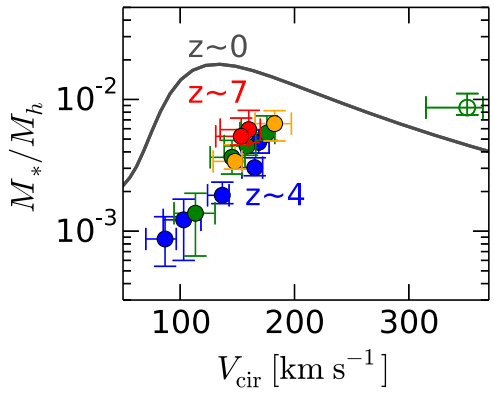

Figure 11. SHMR as a function of circular velocity. The blue, green, orange, and red circles represent the SHMRs of our subsamples at $z \sim 4$, 5, 6, and 7, respectively. The gray solid curve is the SHMR of Behroozi et al. (2013a) at $z \sim 0$.

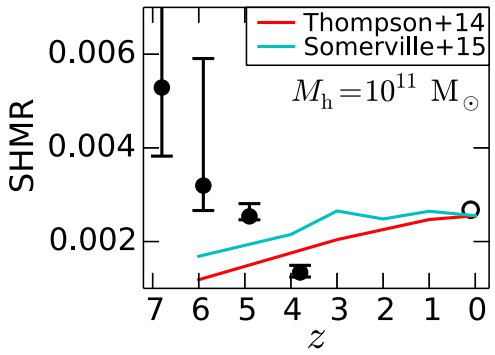

Figure 12. SHMRs predicted by theoretical studies. The red and cyan lines are SHMRs at $M_{\rm h} = 10^{11}$ $M_\odot$ predicted by Thompson et al. (2014) and Somerville et al. (2015), respectively. The black filled and open circles are the SHMRs at $M_{\rm h} = 10^{11}$ $M_\odot$ obtained in this study and in Behroozi et al. (2013a), respectively. To compare the trend with the obtained SHMR evolution, the amplitudes of the red and cyan lines are normalized to the $z \sim 0$ SHMR.

evolution at $z \sim 0$–4 suggests that the early galaxies at $z \sim 4$–7 have gas outflow conditions clearly different from those of mature galaxies at $z \sim 0$.

We compare our SHMRs with results of the theoretical studies and investigate whether the theoretical models explain the SHMR evolution at $z \sim 0$–7. In Figure 12, we plot the SHMRs at $M_{\rm h} = 10^{11}$ $M_\odot$ predicted by the hydrodynamic simulation (Thompson et al. 2014) and the semianalytic model (Somerville et al. 2015). These theoretical studies predict evolutionary trends of the SHMR decrease from $z \sim 0$ to 4 that are similar to our observational results. On the other hand, the theoretical studies cannot reproduce the SHMR increase from $z \sim 4$ to 7 found in our observational study. This discrepancy may pose a challenge in the current theoretical study of galaxy formation.

7.2. Baryon Conversion Efficiency (BCE)

In Section 6.2, we find that SHMR and $M_{\rm h}$ at $z \sim 0$–7 have positive correlations in the mass range around $M_{\rm h} \sim 10^{11}\,M_\odot$ (Figure 9). To understand more details of these positive correlations, we calculate the BCE of the $z \sim 4$ subsamples that have high statistical accuracies. BCE is the ratio of the SFR to the baryon accretion rate, $\dot{M}_{\rm b}$:

$$\mathrm{BCE} = \frac{\mathrm{SFR}}{\dot{M}_{\rm b}}. \quad (64)$$

Because most of the accreting baryons have a form of gas (e.g., Scoville et al. 2015), we adopt $\dot{M}_{\rm g} \simeq \dot{M}_{\rm b}$. Thus, Equation (64) can be written as BCE $\simeq$ SFR/$\dot{M}_{\rm g}$, indicating that BCE is the conversion rate from gas to stars.

We define the cosmic baryon fraction as $f_b \equiv \Omega_{\rm b}/\Omega_{\rm m} = 0.15$. The baryon accretion rate is computed with f_b by

$$\dot{M}_{\rm b} = f_{\rm b} \times \dot{M}_{\rm h}, \quad (65)$$

where $\dot{M}_{\rm h}$ is the median halo mass accretion rate, which is a function of halo mass and redshift. We estimate $\dot{M}_{\rm h}$ with the analytic formula obtained from the N-body simulation results (Behroozi et al. 2013a). The SFRs are derived from the threshold total absolute magnitude in the rest-frame UV band, $M_{\rm UV,th}$. We correct for the dust extinction with two empirical relations. One is the attenuation–UV slope ($\beta_{\rm UV}$) relation

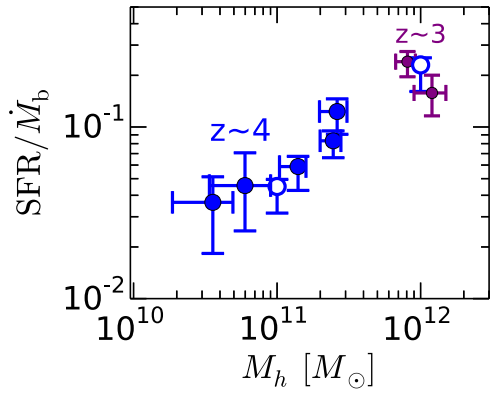

Figure 13. BCE as a function of dark matter halo mass. The blue circles represent the BCEs of our subsample at $z \sim 4$. The open blue circles at $M_{\rm h} = 10^{11}$ and 10^{12} $M_\odot$ describe the BCEs of Behroozi et al. (2013a) at $z \sim 4$. BCEs at $z \sim 3$ (Bian et al. 2013) are shown with purple circles.

(Meurer et al. 1999), and the other is the $\beta_{\rm UV}$–$M_{\rm UV}$ relation (Bouwens et al. 2014).

Figure 13 presents BCEs of our $z \sim 4$ subsamples as a function of the dark matter halo mass. The errors of these BCE estimates do not include the halo mass accretion rate scatters, but the halo mass estimates. Although moderately large uncertainties exist in the results of our $z \sim 4$ subsamples in Figure 13, there is a signature of positive correlation between BCE and $M_{\rm h}$. We compare BCE estimates of Behroozi et al. (2013a) in Figure 13 and confirm that our results including the positive correlation signature are consistent with those of Behroozi et al. (2013a). This consistency would indicate that the abundance matching technique provides results similar to our clustering analysis (see Section 7.3).

This positive correlation signature indicates the low conversion efficiency from gas to stars in low-mass halos, suggesting inefficient star formation in low-mass halos. The inefficient star formation probably originates from the mass dependence of feedback and/or gas cooling. In low-mass halos, star formation activities associated with SNe, stellar wind, and radiation produce outflowing gas that suppresses next-generation star formation as the feedback process. Moreover, in low-mass halos, the gas cooling is slow (Silk & Wyse 1993). The combination of these effects would make the positive correlation between BCE and $M_{\rm h}$.

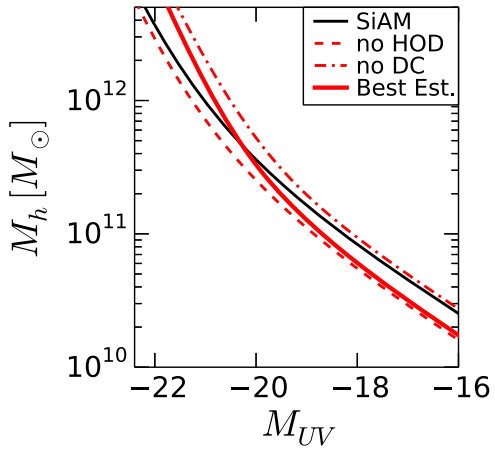

Figure 14. Impact of DC and HOD on the dark matter halo mass estimates. We plot the dark matter halo mass estimates for our $z \sim 4$ subsample as a function of absolute magnitude. The black curve is the result of the simple abundance matching (SiAM). The dashed curve represents the result of the abundance matching with DC = 0.6. The dot–dashed curve denotes the result of the abundance matching considering the HOD ($\sigma_{\log M} = 0.2$, $\log M_0 = 11.5$, $\log M_1' = 12.1$, and $\alpha = 1.0$) with DC = 1.0. The red solid curve is the result of the abundance matching considering the HOD with DC = 0.6, mimicking our clustering analysis results. See Section 7.3.1 for more details.

We compare the BCEs at $z \sim 4$ with those at $z \sim 3$ given by Bian et al. (2013). Because Bian et al. (2013) use the mean halo mass to derive BCEs in their paper, we recalculate BCEs with $M_{\rm min}$ values presented in Bian et al. (2013). We estimate the SFR from the upper limit of the magnitude for each subsample in Bian et al. (2013). We find that the recalculated BCEs of $M_{\rm h} \sim 10^{12}\,M_\odot$ at $z \sim 3$ are comparable to the one at $z \sim 4$ within the error bars (Figure 13).

7.3. Comparisons with Abundance Matching Studies

7.3.1. Impact of DC and HOD Systematics on the M_h Estimates

We discuss differences between our clustering analysis and the abundance matching results. As explained in Section 1, these differences should originate from DC and the subhalo–galaxy relation that are implemented in our HOD model. We investigate the physical impacts of DC and HOD (which affects the subhalo–galaxy relation) on the $M_{\rm h}$ estimates, comparing those obtained from a simple abundance matching (SiAM) method based on halo mass functions of Behroozi et al. (2013a) and UV luminosity functions of Bouwens et al. (2015) at $z \sim 4$. We calculate $M_{\rm h}$ as a function of $M_{\rm UV}$ by the abundance matching technique with and without DC and HOD terms, using

$$\int_0^\infty dM_h' \frac{dn}{dM_h}(M_{\rm h}', z) \times {\rm DC} \times {\rm HOD}(M_{\rm h}', M_{\rm h}) = \int_{M_{\rm UV}}^{-\infty} dM'_{\rm UV}\,\Phi(M'_{\rm UV}, z), \quad (66)$$

where $(dn/dM_h)(M_{\rm h}', z)$ and $\Phi(M_{\rm UV}', z)$ are the halo mass function and the UV luminosity function at $z \sim 4$, respectively. The term of ${\rm HOD}(M_{\rm h}', M_{\rm h})$ is changed on a case-by-case basis, as detailed below.

The calculation results are shown in the $M_{\rm h}$ versus $M_{\rm UV}$ plot of Figure 14. The black solid curve represents the SiAM case that includes neither DC nor the HOD effect, i.e., DC = 1 and ${\rm HOD}(M_{\rm h}', M_{\rm h}) = H(M_{\rm h}' - M_{\rm h})$, where $H(x)$ is a step function. The red dashed curve corresponds to the no-HOD case with the DC effects, DC = 0.6 and ${\rm HOD}(M_{\rm h}', M_{\rm h}) = H(M_{\rm h}' - M_{\rm h})$. The red dot–dashed curve denotes the no-DC case with the HOD effects, DC = 1.0 and ${\rm HOD}(M_{\rm h}', M_{\rm h}) = N_{\rm c}(M_{\rm h}') + N_{\rm s}(M_{\rm h}')$, where we use our best-fit HOD parameter set of the $z \sim 4$ LBG subsample of $m_{\rm UV}^{\rm aper} < 28.2$ mag, which is well determined, $(\sigma_{\log M}, \log M_0, \log M_1', \alpha) = (0.2, 11.5, 12.1, 1.0)$, and $M_{\rm min} = M_{\rm h}$ by definition. The red solid curve indicates the best-estimate case with the DC and HOD effects, mimicking our clustering analysis results, DC = 0.6 and ${\rm HOD}(M_{\rm h}', M_{\rm h}) = N_{\rm c}(M_{\rm h}') + N_{\rm s}(M_{\rm h}')$.

Comparing the best-estimate case with the DC and HOD effects (red solid curve) in Figure 14, we find that the no-DC case (red dot–dashed curve) overestimates $M_{\rm h}$ by $\sim$0.2 dex at the faint magnitude of $M_{\rm UV} \sim -16$ mag. However, this overestimate becomes small at the bright magnitude, suggesting that the DC effect is more important at the faint magnitude. In contrast to the no-DC case, the no-HOD case (red dashed curve) agrees with the best-estimate case (red solid curve) at the faint magnitude, while the no-HOD case underestimates $M_{\rm h}$ by 0.4 dex at the bright magnitude of $M_{\rm UV} = -21.5$ mag. Note that the SiAM case (black solid curve) is bracketed by the no-DC case (red dot–dashed curve) and the no-HOD case (red dashed curve). The SiAM case overestimates (underestimates) $M_{\rm h}$ at the faint (bright) magnitudes by $\sim$0.2 ($\sim$0.4) dex, following the no-DC (no-HOD) case. Because the DC and HOD effects cancel out, the SiAM case provides $M_{\rm h}$ values comparable to those of the best-estimate case at the intermediate magnitude of $M_{\rm UV} \sim -21$ to -20 mag that corresponds to L^*.

7.3.2. Comparisons with the Abundance Matching Results

We compare results of our clustering analyses with those of recent abundance matching studies. Figure 15 presents halo masses estimated by abundance matching techniques of Behroozi et al. (2013a) and Moster et al. (2013), together with our halo mass estimates from the clustering analyses. Here, again, we use the modified results of Behroozi et al. (2013a), whose cosmological parameters and halo mass definition are the same as ours (P. Behroozi 2015, private communication). Figure 16 (Figure 17) is the same as Figure 15, but for Finkelstein et al. (2015), Trac et al. (2015), and Mason et al. (2015) (Mashian et al. 2015). Although the comparisons in the $M_{\rm h}$ versus M_* or SHMR versus $M_{\rm h}$ plot (Figure 15) are straightforward, we use $M_{\rm h}$ versus $M_{\rm UV}$ and $M_{\rm h}$ versus SFR in Figures 16 and 17, respectively. This is because the abundance matching studies shown in Figures 16 and 17 do not present M_*, but $M_{\rm UV}$ or SFR.

In Figure 15, we find that the abundance matching results of Behroozi et al. (2013a) agree with our clustering results at $z \sim$ 5–7 very well within 1σ errors. At $z \sim 4$, the stellar mass range of Behroozi et al. (2013a) does not cover the one of ours, and secure comparisons cannot be made.

Figure 16 indicates that the abundance matching results in Finkelstein et al. (2015) are consistent with our clustering results within 1σ errors at $z \sim$ 5–7, although all of the data of Finkelstein et al. (2015) appear to fall below our clustering results. At $z \sim 4$, the $M_{\rm h}$ values of Finkelstein et al. (2015) are lower than ours by 0.13 dex at $z \sim 4$ at $\sim 2\sigma$ levels. There are similar $\sim 2\sigma$ level $M_{\rm h}$ value offsets of 0.1 ($\sim$0.2) dex to Moster et al. (2013) (Trac et al. 2015; Mashian et al. 2015) at $z \sim 4$ ($z \sim 6$ and 4). The results of Mason et al. (2015) agree well

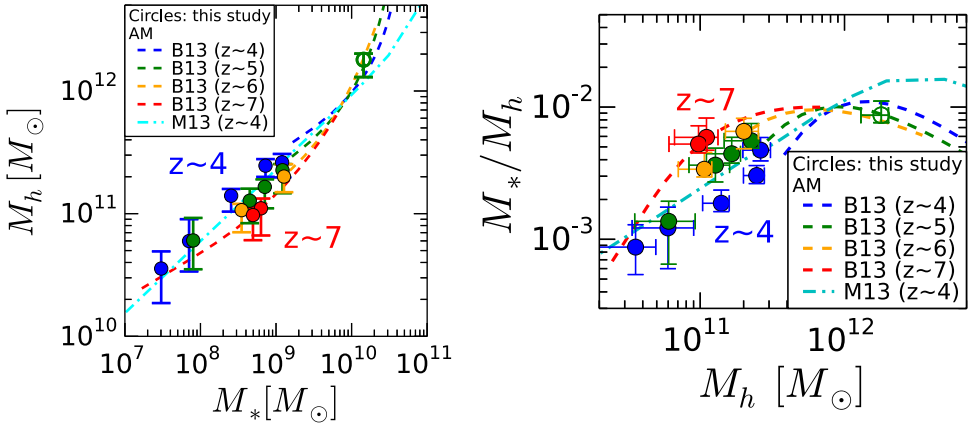

Figure 15. Comparison with Behroozi et al. (2013a) and Moster et al. (2013). Left panel: comparison of the dark matter halo mass as a function of stellar mass. The blue, green, orange, and red dashed curves are the results of Behroozi et al. (2013a). These results are recomputed by P. Behroozi with the same cosmological parameters and halo mass definition as ours. The cyan dot–dashed curve is the result of Moster et al. (2013). The blue, green, orange, and red circles represent the dark matter halo mass of our *Hubble* subsamples at $z \sim 4$, 5, 6, and 7, respectively. The open green circle denotes the dark matter halo mass of our subsample constructed from the HSC data. Right panel: comparison of the SHMR. Same as the left panel, but the horizontal and vertical axes are the dark matter halo mass and the SHMR.

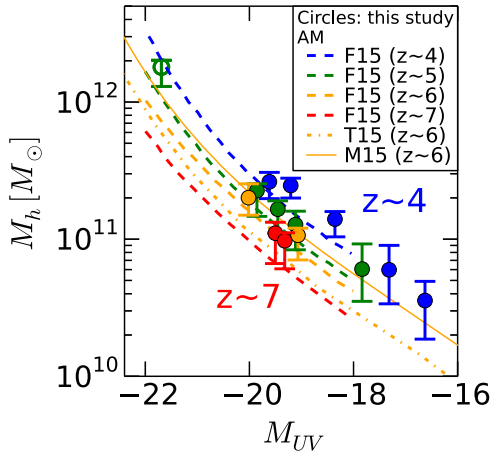

Figure 16. Comparison with Finkelstein et al. (2015), Trac et al. (2015), and Mason et al. (2015). The blue, green, orange, and red dashed curves are the results of Finkelstein et al. (2015) at $z \sim 4$, 5, 6, and 7, respectively. The orange dot–dashed and solid curves shows the $z \sim 6$ results of Trac et al. (2015) and Mason et al. (2015), respectively. The blue green, orange, and red circles represent the dark matter halo masses of our subsamples at $z \sim 4$, 5, 6, and 7, respectively.

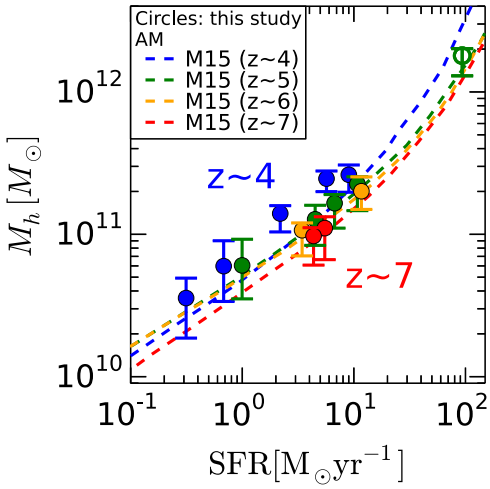

Figure 17. Comparison with Mashian et al. (2015). The blue, green, orange, and red dashed curves are the results of Mashian et al. (2015) at $z \sim 4$, 5, 6, and 7, respectively. The blue, green, orange, and red circles represent the dark matter halo masses of our subsamples at $z \sim 4$, 5, 6, and 7, respectively.

with ours within the error bars. Note that all of these studies adopt cosmological parameters different from ours. The cosmological parameter sets used in Moster et al. (2013), Trac et al. (2015), Mashian et al. (2015), and Mason et al. (2015) are $(H_0, \Omega_m, \Omega_\Lambda, \sigma_8) = (70.4, 0.272, 0.728, 0.810)$, (70, 0.27, 0.73, 0.8), (70, 0.3, 0.7, 0.82), and (67.31, 0.315, 0.685, 0.829), respectively. Finkelstein et al. (2015) use the parameter sets of $(H_0, \Omega_m, \Omega_\Lambda) = (70.2, 0.275, 0.725)$. If we correct these study results for the effects of the different cosmological parameters, the DC, and the halo mass function, these study results agree with our clustering analysis estimates within ∼0.1 dex. In other words, all of these abundance matching results agree with our clustering results very well. In Section 7.3.1, we compare the results of SiAM with those of the best estimates having clustering analysis parameter constraints, and we conclude that the SiAM results differ from the best estimates up to 0.4 dex in M_h. However, we find very good agreements between the recent abundance matching studies and the clustering analysis study, within ∼0.1 dex in M_h. These good agreements are probably explained by the fact that these abundance matching studies are different from the classical technique of SiAM, but with subhalos, incompleteness (similar to DC; Behroozi et al. 2013a), and/or SFR+stellar mass function evolution that reduce the systematics.

7.3.3. Conclusions of the Comparisons

In Section 7.3.2, we find that M_h estimates from our clustering analyses agree with most of the abundance matching results within the ∼0.1 dex level at $z \sim 4$–7, which are corrected for the differences of cosmological parameters, the DC values, and the halo mass functions. Although systematic M_h differences exist originating from the DC and HOD uncertainties up to about 0.4 dex or a factor of 3 in the SiAM at the dark matter halo mass of 10^{10}–10^{12} $M_\odot$ (Section 7.3.1), the recent abundance matching techniques including the subhalos, incompleteness, and/or SFR+stellar-mass evolution appear to reduce the systematics down to the ∼0.1 dex level. Thus, the abundance matching techniques are useful to estimate M_h of

high-z galaxy halos, if one allows the systematic uncertainties up to a factor of 3. The good agreements between the clustering and abundance matching techniques are found probably because the systematics of the subhalo–galaxy relation is small due to the small satellite fraction at high z (Zheng et al. 2007; Coupon et al. 2012; see also Jaacks et al. 2015).

8. SUMMARY

We obtain clustering measurements of $z \sim 4$–7 galaxies from the data set of the legacy deep *Hubble*/ACS and WFC3 images and the complimentary large-area Subaru/HSC images that are newly available. Via our HOD modeling, we investigate SHMRs at $z \sim 4$–7 for the first time by galaxy clustering analyses. We compare our clustering analysis results with the abundance matching results that are actively being obtained by recent studies. Our major findings are summarized below.

1. The mean dark matter halo masses of our LBGs at $z \sim 4$–7 are $\langle M_{\rm h}\rangle \sim (1-20) \times 10^{11}\ M_\odot$. There is an increasing trend in the dark matter halo mass with increasing UV luminosity of LBGs at $z \sim 4$–7. Our estimated dark matter halo masses are consistent with the previous clustering studies in the $\langle M_{\rm h}\rangle$–$\langle M_{\rm UV}\rangle$ plane, if we use the same cosmological parameter set for comparison.
2. We estimate SHMR for our LBGs. We identify the SHMR evolutions in $z \sim 0$–4 and $z \sim 4$–7 at the >98% confidence level for the first time based on clustering analyses. We find that, at the dark matter halo mass of $M_{\rm h} \sim 10^{11}\ M_\odot$, SHMRs decrease by a factor of ∼2, from $\sim 2.7 \times 10^{-3}$ ($z \sim 0$) to $\sim 1.3 \times 10^{-3}$ ($z \sim 4$), and increase by a factor of ∼4, from $\sim 1.3 \times 10^{-3}$ ($z \sim 4$) to $\sim 5.3 \times 10^{-3}$($z \sim 7$).
3. We compare our SHMRs with results of the hydrodynamic simulation and the semianalytic model at $M_{\rm h} = 10^{11}\ M_\odot$. These theoretical studies predict evolutionary trends of the SHMR decrease from $z \sim 0$ to 4 that are similar to our observational results. On the other hand, the theoretical studies cannot reproduce the SHMR increase from $z \sim 4$ to 7 found in our observational study.
4. We calculate BCE, which is the ratio of the SFR to the baryon accretion rate, corresponding to rates of the conversion from gas to stars. The BCEs at $z \sim 4$ increase from $\sim 3 \times 10^{-2}$ to $\sim 1 \times 10^{-1}$ with increasing dark matter halo mass up to $\sim 10^{12}\ M_\odot$. The low-mass halos form stars inefficiently, probably due to feedback effects and/or slow gas cooling.
5. We compare our clustering+HOD results with abundance matching estimates. We find that the $M_{\rm h}$ estimates of clustering+HOD analyses agree with those of the SiAM within a factor of 3. Moreover, the results of the recent studies' sophisticated abundance matching techniques including the subhalos, incompleteness, and/or SFR +stellar-mass evolution are even better than those of the SiAM technique, some of which agree with our clustering results within 0.1 dex at $z \sim 4$–7. Due to the small galaxy occupation in one halo at high z, abundance matching techniques are useful to estimate $M_{\rm h}$, if one allows these reasonably small uncertainties raised by the assumptions of the abundance matching techniques.

We thank the anonymous referee for a careful reading and valuable comments that improved the clarity of the paper. We are grateful to Peter Behroozi for useful discussions and providing his SHMR results, which are recalculated with the same cosmological parameters and halo mass definition as ours. We appreciate helpful comments on an early draft version of this paper from Michael A. Strauss and Masahiro Takada. We thank Jim Bosch, Hisanori Furusawa, Robert H. Lupton, Sogo Mineo, and Naoki Yasuda for their helpful comments and discussions on the treatment of the HSC data. We are also grateful to Masayuki Tanaka for kindly providing a masking code and discussing our results. This work has benefited from many interesting conversations with Renyue Cen, Motohiro Enoki, Thibault Garel, Ryosuke Goto, Masao Hayashi, Chiaki Hikage, Yutaka Hirai, Soh Ikarashi, Akio Inoue, Masaru Kajisawa, Nobunari Kashikawa, Daichi Kashino, Charlotte A. Mason, Masakazu A. R. Kobayashi, Masato I. N. Kobayashi, Andrei Mesinger, Kentaro Nagamine, Tohru Nagao, Masahiro Nagashima, Atsushi J. Nishizawa, Takashi Okamoto, Kouji Ohta, Taku Okamura, Jaehong Park, Yoshiaki Sofue, Guochao Sun, Tsutomu Takeuchi, and Masayuki Umemura.

This work is based on observations taken by the 3D-*HST* Treasury Program (GO 12177 and 12328) and CANDELS Multi-Cycle Treasury Program with the NASA/ESA *HST*, which is operated by the Association of Universities for Research in Astronomy, Inc., under NASA contract NAS5-26555. This paper makes use of software developed for the Large Synoptic Survey Telescope. We thank the LSST Project for making their code available as free software at http://dm.lsstcorp.org.

The Pan-STARRS1 Surveys (PS1) have been made possible through contributions of the Institute for Astronomy, the University of Hawaii, the Pan-STARRS Project Office, the Max-Planck Society and its participating institutes, the Max Planck Institute for Astronomy, Heidelberg, and the Max Planck Institute for Extraterrestrial Physics, Garching, Johns Hopkins University, Durham University, the University of Edinburgh, Queen's University Belfast, the Harvard-Smithsonian Center for Astrophysics, the Las Cumbres Observatory Global Telescope Network Incorporated, the National Central University of Taiwan, the Space Telescope Science Institute, the National Aeronautics and Space Administration under Grant No. NNX08AR22G issued through the Planetary Science Division of the NASA Science Mission Directorate, the National Science Foundation under Grant No. AST-1238877, the University of Maryland, and Eotvos Lorand University (ELTE).

This work is supported by World Premier International Research Center Initiative (WPI Initiative), MEXT, Japan, KAKENHI (23244025) and (15H02064) Grant-in-Aid for Scientific Research (A) through Japan Society for the Promotion of Science (JSPS), and a grant from the Hayakawa Satio Fund awarded by the Astronomical Society of Japan. Y.H. is supported by an Advanced Leading Graduate Course for Photon Science grant (ALPS) and the JSPS Research Fellowship for Young Scientists. S.M. is supported by KAKENHI (15K17600).

Facilities: HST (ACS, WFC3), Subaru (HSC, Suprime-Cam), CFHT (MEGACAM).

REFERENCES

Adelberger, K. L., Steidel, C. C., Pettini, M., et al. 2005, ApJ, 619, 697
Alam, S., Albareti, F. D., Allende Prieto, C., et al. 2015, ApJS, 219, 12

Axelrod, T., Kantor, J., Lupton, R. H., & Pierfederici, F. 2010, Proc. SPIE, 7740, 15
Barone-Nugent, R. L., Trenti, M., Wyithe, J. S. B., et al. 2014, ApJ, 793, 17
Bartelmann, M., & Schneider, P. 2001, PhR, 340, 291
Beckwith, S. V. W., Stiavelli, M., Koekemoer, A. M., et al. 2006, AJ, 132, 1729
Behroozi, P. S., Conroy, C., & Wechsler, R. H. 2010, ApJ, 717, 379
Behroozi, P. S., Wechsler, R. H., & Conroy, C. 2013a, ApJ, 770, 57
Behroozi, P. S., Wechsler, R. H., & Wu, H.-Y. 2013b, ApJ, 762, 109
Berlind, A. A., & Weinberg, D. H. 2002, ApJ, 575, 587
Berlind, A. A., Weinberg, D. H., Benson, A. J., et al. 2003, ApJ, 593, 1
Bertin, E., & Arnouts, S. 1996, A&AS, 117, 393
Bertin, E., Mellier, Y., Radovich, M., et al. 2002, in ASP Conf. Ser. 281, Astronomical Data Analysis Software and Systems XI, ed. D. A. Bohlender, D. Durand, & T. H. Handley (San Francisco, CA: ASP), 228
Bian, F., Fan, X., Jiang, L., et al. 2013, ApJ, 774, 28
Birrer, S., Lilly, S., Amara, A., Paranjape, A., & Refregier, A. 2014, ApJ, 793, 12
Blanton, M. R., & Roweis, S. 2007, AJ, 133, 734
Bouwens, R. J., Illingworth, G. D., Oesch, P. A., et al. 2010, ApJL, 708, L69
Bouwens, R. J., Illingworth, G. D., Oesch, P. A., et al. 2011, ApJ, 737, 90
Bouwens, R. J., Illingworth, G. D., Oesch, P. A., et al. 2014, ApJ, 793, 115
Bouwens, R. J., Illingworth, G. D., Oesch, P. A., et al. 2015, ApJ, 803, 34
Brammer, G. B., van Dokkum, P. G., Franx, M., et al. 2012, ApJS, 200, 13
Bruzual, G., & Charlot, S. 2003, MNRAS, 344, 1000
Bullock, J. S., Kolatt, T. S., Sigad, Y., et al. 2001, MNRAS, 321, 559
Bullock, J. S., Wechsler, R. H., & Somerville, R. S. 2002, MNRAS, 329, 246
Calzetti, D., Armus, L., Bohlin, R. C., et al. 2000, ApJ, 533, 682
Chabrier, G. 2003, PASP, 115, 763
Conroy, C., Wechsler, R. H., & Kravtsov, A. V. 2006, ApJ, 647, 201
Cooray, A., & Sheth, R. 2002, PhR, 372, 1
Coupon, J., Arnouts, S., van Waerbeke, L., et al. 2015, MNRAS, 449, 1352
Coupon, J., Kilbinger, M., McCracken, H. J., et al. 2012, A&A, 542, A5
Daddi, E., Dickinson, M., Morrison, G., et al. 2007, ApJ, 670, 156
Dekel, A., Birnboim, Y., Engel, G., et al. 2009, Natur, 457, 451
Durkalec, A., Le Fèvre, O., de la Torre, S., et al. 2015, A&A, 576, L7
Efstathiou, G., Bernstein, G., Tyson, J. A., Katz, N., & Guhathakurta, P. 1991, ApJL, 380, L47
Ellis, R. S., McLure, R. J., Dunlop, J. S., et al. 2013, ApJL, 763, L7
Erb, D. K., Steidel, C. C., Shapley, A. E., et al. 2006, ApJ, 646, 107
Fakhouri, O., Ma, C.-P., & Boylan-Kolchin, M. 2010, MNRAS, 406, 2267
Finkelstein, S. L., Song, M., Behroozi, P., et al. 2015, arXiv:1504.00005
Fisher, K. B., Davis, M., Strauss, M. A., Yahil, A., & Huchra, J. P. 1994, MNRAS, 267, 927
Foucaud, S., Conselice, C. J., Hartley, W. G., et al. 2010, MNRAS, 406, 147
Foucaud, S., McCracken, H. J., Le Fèvre, O., et al. 2003, A&A, 409, 835
Garel, T., Blaizot, J., Guiderdoni, B., et al. 2015, MNRAS, 450, 1279
Grogin, N. A., Kocevski, D. D., Faber, S. M., et al. 2011, ApJS, 197, 35
Groth, E. J., & Peebles, P. J. E. 1977, ApJ, 217, 385
Guo, H., Zheng, Z., Behroozi, P. S., et al. 2015, arXiv:1508.07012
Hamana, T., Ouchi, M., Shimasaku, K., Kayo, I., & Suto, Y. 2004, MNRAS, 347, 813
Harikane, Y., Ouchi, M., Yuma, S., et al. 2014, ApJ, 794, 129
Hatfield, P. W., Lindsay, S. N., Jarvis, M. J., et al. 2015, arXiv:1511.05476
Hildebrandt, H., Pielorz, J., Erben, T., et al. 2007, A&A, 462, 865
Hildebrandt, H., Pielorz, J., Erben, T., et al. 2009, A&A, 498, 725
Hopkins, P. F., Kereš, D., Oñorbe, J., et al. 2014, MNRAS, 445, 581
Hudson, M. J., Gillis, B. R., Coupon, J., et al. 2015, MNRAS, 447, 298
Illingworth, G. D., Magee, D., Oesch, P. A., et al. 2013, ApJS, 209, 6
Ishigaki, M., Kawamata, R., Ouchi, M., et al. 2015, ApJ, 799, 12
Ishikawa, S., Kashikawa, N., Hamana, T., Toshikawa, J., & Onoue, M. 2016, MNRAS, arXiv:1602.01845
Ishikawa, S., Kashikawa, N., Toshikawa, J., & Onoue, M. 2015, MNRAS, 454, 205
Ivezic, Z., Tyson, J. A., Abel, B., et al. 2008, arXiv:0805.2366
Iye, M., Karoji, H., Ando, H., et al. 2004, PASJ, 56, 381
Jaacks, J., Finkelstein, S. L., & Nagamine, K. 2015, arXiv:1507.00713
Jee, M. J., & Tyson, J. A. 2011, PASP, 123, 596
Kawamata, R., Ishigaki, M., Shimasaku, K., Oguri, M., & Ouchi, M. 2015, ApJ, 804, 103
Kereš, D., Katz, N., Davé, R., Fardal, M., & Weinberg, D. H. 2009, MNRAS, 396, 2332
Koekemoer, A. M., Ellis, R. S., McLure, R. J., et al. 2013, ApJS, 209, 3
Koekemoer, A. M., Faber, S. M., Ferguson, H. C., et al. 2011, ApJS, 197, 36
Kravtsov, A. V., Berlind, A. A., Wechsler, R. H., et al. 2004, ApJ, 609, 35
Landy, S. D., & Szalay, A. S. 1993, ApJ, 412, 64
Leauthaud, A., Tinker, J., Behroozi, P. S., Busha, M. T., & Wechsler, R. H. 2011, ApJ, 738, 45
Leauthaud, A., Tinker, J., Bundy, K., et al. 2012, ApJ, 744, 159
Lee, K.-S., Giavalisco, M., Conroy, C., et al. 2009, ApJ, 695, 368
Lee, K.-S., Giavalisco, M., Gnedin, O. Y., et al. 2006, ApJ, 642, 63
Ling, E. N., Barrow, J. D., & Frenk, C. S. 1986, MNRAS, 223, 21P
Magnier, E. A., Schlafly, E., Finkbeiner, D., et al. 2013, ApJS, 205, 20
Mandelbaum, R., Seljak, U., Kauffmann, G., Hirata, C. M., & Brinkmann, J. 2006, MNRAS, 368, 715
Martinez-Manso, J., Gonzalez, A. H., Ashby, M. L. N., et al. 2015, MNRAS, 446, 169
Mashian, N., Oesch, P., & Loeb, A. 2015, arXiv:1507.00999
Mason, C., Trenti, M., & Treu, T. 2015, arXiv:1508.01204
McBride, C., Berlind, A., Scoccimarro, R., et al. 2009, BAAS, 41, 253
McCracken, H. J., Wolk, M., Colombi, S., et al. 2015, MNRAS, 449, 901
Meurer, G. R., Heckman, T. M., & Calzetti, D. 1999, ApJ, 521, 64
Mitchell, P., Lacey, C., Baugh, C., & Cole, S. 2015, arXiv:1510.08463
Miyazaki, S., Komiyama, Y., Nakaya, H., et al. 2012, Proc. SPIE, 8446, 0
Mo, H. J., Jing, Y. P., & Boerner, G. 1992, ApJ, 392, 452
More, S., Miyatake, H., Mandelbaum, R., et al. 2015, ApJ, 806, 2
More, S., van den Bosch, F. C., Cacciato, M., et al. 2011, MNRAS, 410, 210
Moster, B. P., Naab, T., & White, S. D. M. 2013, MNRAS, 428, 3121
Murray, N., Quataert, E., & Thompson, T. A. 2005, ApJ, 618, 569
Navarro, J. F., Frenk, C. S., & White, S. D. M. 1996, ApJ, 462, 563
Navarro, J. F., Frenk, C. S., & White, S. D. M. 1997, ApJ, 490, 493
Okamoto, T., Shimizu, I., & Yoshida, N. 2014, PASJ, 66, 70
Oke, J. B., & Gunn, J. E. 1983, ApJ, 266, 713
Ouchi, M., Hamana, T., Shimasaku, K., et al. 2005, ApJL, 635, L117
Ouchi, M., Shimasaku, K., Furusawa, H., et al. 2010, ApJ, 723, 869
Ouchi, M., Shimasaku, K., Okamura, S., et al. 2001, ApJL, 558, L83
Ouchi, M., Shimasaku, K., Okamura, S., et al. 2004a, ApJ, 611, 660
Ouchi, M., Shimasaku, K., Okamura, S., et al. 2004b, ApJ, 611, 685
Park, J., Kim, H.-S., Wyithe, J. S. B., et al. 2015, arXiv:1511.01983
Peebles, P. J. E. 1980, The Large-scale Structure of the Universe (Princeton, NJ: Princeton Univ. Press)
Reddick, R. M., Wechsler, R. H., Tinker, J. L., & Behroozi, P. S. 2013, ApJ, 771, 30
Rees, M. J., & Ostriker, J. P. 1977, MNRAS, 179, 541
Roche, N., & Eales, S. A. 1999, MNRAS, 307, 703
Rodríguez-Puebla, A., Avila-Reese, V., Yang, X., et al. 2015, ApJ, 799, 130
Saito, S., Leauthaud, A., Hearin, A. P., et al. 2015, arXiv:1509.00482
Salpeter, E. E. 1955, ApJ, 121, 161
Schlafly, E. F., Finkbeiner, D. P., Jurić, M., et al. 2012, ApJ, 756, 158
Scoville, N., Sheth, K., Aussel, H., et al. 2015, arXiv:1505.02159
Seljak, U. 2000, MNRAS, 318, 203
Shan, H., Kneib, J.-P., Li, R., et al. 2015, arXiv:1502.00313
Shibuya, T., Ouchi, M., & Harikane, Y. 2015, arXiv:1503.07481
Shimizu, M., Kitayama, T., Sasaki, S., & Suto, Y. 2003, ApJ, 590, 197
Silk, J., & Wyse, R. F. G. 1993, PhR, 231, 293
Skelton, R. E., Whitaker, K. E., Momcheva, I. G., et al. 2014, ApJS, 214, 24
Skibba, R. A., Coil, A. L., Mendez, A. J., et al. 2015, ApJ, 807, 152
Sofue, Y. 2015, PASJ, arXiv:1510.05752
Somerville, R. S., Lee, K., Ferguson, H. C., et al. 2004, ApJL, 600, L171
Somerville, R. S., Popping, G., & Trager, S. C. 2015, MNRAS, 453, 4337
Song, M., Finkelstein, S. L., Ashby, M. L. N., et al. 2015, arXiv:1507.05636
Speagle, J. S., Steinhardt, C. L., Capak, P. L., & Silverman, J. D. 2014, ApJS, 214, 15
Steidel, C. C., Adelberger, K. L., Giavalisco, M., Dickinson, M., & Pettini, M. 1999, ApJ, 519, 1
Steinhardt, C. L., Speagle, J. S., Capak, P., et al. 2014, ApJL, 791, L25
Sutherland, R. S., & Dopita, M. A. 1993, ApJS, 88, 253
Thompson, R., Nagamine, K., Jaacks, J., & Choi, J.-H. 2014, ApJ, 780, 145
Tinker, J., Kravtsov, A. V., Klypin, A., et al. 2008, ApJ, 688, 709
Tinker, J. L., Robertson, B. E., Kravtsov, A. V., et al. 2010, ApJ, 724, 878
Tonry, J. L., Stubbs, C. W., Lykke, K. R., et al. 2012, ApJ, 750, 99
Trac, H., Cen, R., & Mansfield, P. 2015, arXiv:1507.02685
van den Bosch, F. C., More, S., Cacciato, M., Mo, H., & Yang, X. 2013, MNRAS, 430, 725
Whitaker, K. E., Franx, M., Leja, J., et al. 2014, ApJ, 795, 104
Yagi, M., Kashikawa, N., Sekiguchi, M., et al. 2002, AJ, 123, 66
Zehavi, I., Zheng, Z., Weinberg, D. H., et al. 2005, ApJ, 630, 1
Zheng, Z., Berlind, A. A., Weinberg, D. H., et al. 2005, ApJ, 633, 791
Zheng, Z., Coil, A. L., & Zehavi, I. 2007, ApJ, 667, 760